Computational Aeroacoustic Modelling Using Hybrid RANS/LES Methods With Modified Acoustic Analogies

Zamashobane Nyandeni

June 21, 2017

Supervised by:

Dr Tiri Chinyoka
Centre for Research in Computational and Applied Mechanics
University of Cape Town
Tiri.Chinyoka@uct.ac.za

Abstract

This study considers a numerical approach to identifying noise mechanisms in tandem cylinders to understand aircraft landing gear as a primary contributor to airframe noise during approach and landing. Fluctuations in the flow properties induced by turbulence are computed as well as the corresponding propagations. A hybrid IDDES turbulence model is employed, to compute the boundary layer and fluctuations in the flow properties. Larsson et al. [1] modified Curle's analogy leading to the derivation of a version of Curle's analogy that makes use of strictly time derivatives which has been proven to be less sensitive to numerical errors. Brentner and Farassat [2] derived a formulation of the Ffowcs-Williams and Hawkings analogy for a permeable surface enclosing the acoustic sources which accounts for the quadrupole acoustic sources in the flow without the costly calculation of a volume integral. This study will consider the impact of neglecting the volume sources through a comparison of the two modified versions of Curle's and FWH analogies with the results of other CFD practitioners as well as experimental data.

Dissertation presented for the degree of Master of Science in the department of
Mathematics and Applied Mathematics
University of Cape Town

I know the meaning of plagiarism and declare that all of the work in the dissertation, save for that which is properly acknowledged, is my own.

Signed: Zamashobane Nyandeni Date: 13/03/2017

Acknowledgements

I am truly humbled by the support I have received throughout the duration of this masters. To my beloved mothers, Noluthando and Nandipha, you have my gratitude for being my pillars of strength throughout this testing period. Your love and support has been invaluable. Ndyanithanda. Ndiyabulela Manyawuza. To my brother and father, were it not for your militance and unwavering support, I would not even have made it to university let alone completing this masters. Thank you for always being there for me and for making sure I make it to Cape Town in one piece. I love you guys deeply. Ngiyabonga Gasela, Vumisa, Khukhuza ka Ngonyama ka Mashobane.

To Dr Tirivanhu Chinyoka, for the support he has provided throughout this period, for the personal sacrifices as well as the battles he has waged on my behalf I give thanks. You ensured I have ample resources at my disposal which has aided me to reach this point. I will always be grateful.

To Dr Johan Heyns I would like to give thanks for introducing me to the fascinating world of aeroacoustics. The time and effort you have invested in this disertation is greatly valued. Your guidance and patience was the light I needed through the good times and the bad. Thank you so much Johan.

To the National Research Foundation, The Council for Scientific and Industrial Research, and The Armaments Corporation of South Africa I extend thanks for the financial and technical support required for the completion of this work.

Special thanks are due to Andrew Gill and Charles Crosby from The Centre for High Performance Computing. Your time and support is greatly appreciated and acknowledged.

To all the family I connected with while in Cape Town. Thank you for the part you have played in this chapter of my life. I will always remember you.

Nomenclature

Abbreviations

2-D	Two dimensional
3-D	Three dimensional
CAA	Computational aeroacoustics
CFD	Computational fluid dynamics
CFL	Courant-Friedrichs-Lewy
dB	Decibels
DDES	Delayed detached eddie simulation
DES	Detached eddie simulation
DNS	Direct numerical simulation
DS	Direct simulation
FW-H	Ffowcs-Williams and Hawkings
Hz	Hertz
LaRC	NASA's Langley Research Center
LES	Large eddie simulation
OASPL	Overall sound pressure level
PSD	Power spectral density
RANS	Reynolds averaged Navier-Stokes
RANS/LES	Hybrid RANS and LES model
SA	Spalart-Almaras
SA-DDES	Spalart-Almaras delayed detached eddie simulation
SA-IDDES	Spalart-Almaras improved DDES
SGS	Sub-grid scale

SPL	Sound pressure level
SST	Shear stress tensor
URANS	Unsteady Reynolds averaged Navier-Stokes

Dimensionless Quantities

C_D	Drag coefficient
C_f	skin friction coeffcient
C_L	Lift coefficient
C_p	Pressure coefficient
Re	Reynolds number
St	Strouhal number
u^+	Normalised stream wise velocity
y^+	Wall-normal distance (inner region)

Geometric Quantities

$\mathbf{x}$	Observation co-ordinate
$\mathbf{y}$	Source co-ordinate
A_f	Face area
D	Cavity depth or cylinder diameter
$f\left(\mathbf{x}, t\right)$	Moving surface
L	Cavity length
l_i	Unit vector pointing from surface to observer
n_i	Unit surface normal pointing outward
r	Distance from source to observer
S	Distance between cylinder centres
V	Cell volume
x_i	Cartesian tensor coordinate

y_i	Cartesian tensor coordinate of source location

Latin Symbols/Quantities

f	Frequency
M	Mach number
M_r	Mach number in radiation direction
t	Time
T_{ij}	Lighthill's tensor
u_τ	Friction velocity
u_i	Instantaneous velocity
v_n	surface velocity

Mathematical Symbols

$\bar{f}$	Spatially filtered quantity or spatial average
$\dot{f}$	Time derivative
f'	Fluctuating quantity
f_{RMS}	Root mean square
$H(f)$	Heaviside function

Greek Symbols/Quantities

Δf	Frequency step
Δt	Time step
$\Delta x, \Delta y, \Delta z$	Streamwise,vertical and spanwise spatial step
$\delta(f)$	Dirac's delta function
δ_{ij}	Kronecker delta function
μ	Dynamic viscosity
ν	Kinematic viscosity
ρ	Density

τ_{ij}	Viscous stress tensor
τ	Retarded time
τ_w	Wall shear stress
θ	Momentum thickness

Thermodynamic Quantities

c_0	Speed of sound
p	Pressure

Contents

List of Figures

1 Introduction

1.1 Why The Aviation Industry Is Interested In Reducing Noise

The increase in population density near airports has placed emphasis on limiting the health risks associated with noise. This will require aircrafts of the future to reduce emitted noise signatures, consequently, the attempt to understand and reduce airframe noise has become an important research topic. The physical understanding obtained from these efforts has resulted in the development of hardware capable of reducing noise and adhering to strict noise certification requirements determined by the International Civil Aviation Organization (ICAO), these can be found in their published Environmental Technical Manual, Annex 16 [19].

Rlumenthal et al. [20] from Boeing reviewed aircraft environmental problems in the early 1970s. Due to the introduction of quieter engines they discovered a new problem for future aircraft designers to consider, namely, airframe noise, defined to be the scattering of non-linear disturbances into sound. They subsequently demonstrated that the high-lift devices and landing gear could contribute as much as 10-12 decibls(dB) to the effective perceived noise level of the aircraft on approach and landing. Since aircraft landing gear have been identified as dominant emitters of noise signatures, the study and subsequent attenuation of landing gear noise through design modifications is valuable in terms of reducing the overall aircraft landing noise.

1.2 Aeroacoutsics

Aeroacoustics is the field that studies flow-induced sound, mainly applied in research dedicated to understanding and reducing the noise emitted by aircrafts, industrial heat exchangers and architectural designs [14]. Aeroacoustic problems are classified based on the physical processes responsible for the sound radiation. These range between linear problems of radiation, refraction, and scattering by solid bodies, to non-linear problems such as sound generation due to turbulence, which will form a fundamental part of the study [21]. In order to understand noise mechanisms produced by flows; theoretical, experimental and computational aeroacoustic studies of noise signatures must take place.

According to Hubbard [22]; through study of theoretical, experimental and computational aeroacoustics, in some instances engineers have been able to reduce overall sound pressure level by 20-30 dB for some types of power plants, while in the same period increasing their installed power significantly. It is practice to base the approaches on those generally used in computational fluid dynamics, CFD, but it should be noted that the nature, characteristics and objectives of aeroacoustic problems are indeed different from common CFD problems hence there are computational issues that are unique to aeroacoustics [21].

To reliably develop numerical methods for sound generation and propagation problems, the characteristics of sound generation and propagation problems must be rigorously accounted for through study. The use of computational approaches can be used for noise prediction and therefore are desired if optimal designs are to be discovered inexpensively and subsequently implemented [22]. The main reason why the numerical approach to aeroacoustics is preferred to the experimental approach; is the relative ease it provides designers to assess different configurations and to identify possible deficiencies early during the design process [23]. Even though the experimental approach gives actual noise levels, it is expensive to evaluate a large number of configurations and it can only be performed much later in the development process. The numerical approach, however, is an approximation and will need to be validated against experimental data or analytical solutions to ensure the fidelity of the numerical implementation.

1.3 Overview

This study considers the computational approach to obtaining acoustic sound sources, which involves the numerical prediction of aerodynamic performance using unsteady zonal hybrid RANS/LES simulations to provide a comprehensive description of the unsteady flow, these will be discussed in greater detail in chapter 2. In order to capture sound sources from flows the aeroacoustic characteristics are predicted using analytical (integral) methods. Industry and academic approaches will be discussed in chapter 2 and subsequently derived in chapter 3. Details regarding the numerical implementation of the CFD and CAA methods are included in chapter 4. Chapter 5 presents a verification and validation of the the numerical implementation applied to two test cases, namely, an open-cavity and cylinders in tandem. Subsequently, chapter 6 presents insights and recommendations for future work.

Figure 1: Landing gear noise has been proven to be a dominant airframe noise contributor for wide-body aircraft, whereas for medium size aircraft the noise from the high lift devices dominated [3] and [4].

2 Literature Review

2.1 Overview

This chapter presents a review of literature relevant to the current research. This incorporates a large range of subjects pertinent to tandem cylinder and landing gear aeroacoustic research. Various noise prediction methods are reviewed along with numerical methods and studies pertinent to the current research.

2.2 Introduction

Full scale Airbus A340 landing gear wind tunnel tests as well as full flight tests were completed by Dobrzynski et al. [4] and Chow et al. [3]. It was found that the Landing gear noise is a dominant airframe noise contributor for wide-body aircraft, whereas for medium size aircraft the noise from the high lift devices dominated.

Gibson [24] investigated non-engine aerodynamic noise of a large aircraft. It was found that both the landing gear and the flaps generated significant low-frequency noise. The noise from landing gear is broadband across a large frequency range. High-frequency noise is generally caused by small details on the landing gear and is non-trivial [6]. Lockard et al [18] discuss experimental investigations on cylinders in tandem. They highlight the main features of the generated sound spectrum are humps in the low frequency range between 20Hz $<$ f $<$ 1kHz, low frequency band tonal and broadband noise.

The noise generated by flows about cylinders in tandem configuration is important because it occurs in a wide variety of applications that include aircraft landing gear such as the gear depicted in figure 1. The tandem cylinder configuration represents several component interactions on real landing gear and is regarded as the most fundamental geometry that can be used to model and analyse the physical mechanisms involved in component interaction noise [6]. One of the objectives of this study is to gain a better understanding of various acoustic modelling techniques in order to make recommendations on how they can be applied in the future when more realistic cases are considered. Recent increases in computational power has allowed CFD to be applied to full landing gear geometries, however, due to the objective of evaluating different methodologies, the landing gear geometry in this study must be simplified. As soon as the restrictions of each methodology is understood, a full geometry can be considered.

When the cylinders are close to one another, vortex shedding from the upstream cylinder has been found to be suppressed when the cylinder spacing is increased, various phenomena take place [17]. An example of interest is upstream shear layer reattachment occurring on the downstream cylinder [15]. The subsequent impingement of the wake on the downstream body creates high amplitude unsteady forces and intense radiated noise [15].

Significant sources of noise are prevalent from the interaction of unsteady flow fields with geometric inhomogeneities. These noise sources can be understood as the transformation of the energy generated due to vorticity into acoustical energy [25]. To numerically model these noise producing vortices a variety of approaches are available. These will be discussed in detail in the next sections.

2.3 Direct Acoustic Computation using DNS or LES

Direct acoustic computation solves the compressible Navier-Stokes equations and obtains acoustic sources without modeling, making it the most straightforward way to compute sound because the governing equations completely describe all motions in a fluid which includes acoustic phenomena [1]. Due to the extreme computational cost of performing a direct acoustic computation it has only been solved for academic test cases. The whole range of length scales, from the Kolmogorov microscale to the distance traveled by the sound waves, needs to be resolved, which makes the method more expensive than traditional, incompressible, Direct Numerical Simulation (DNS).

The fact that different physical (turbulent and acoustic) phenomena have to be resolved results in high accuracy requirements on the numerical modelling. In DNS it is common to use higher order schemes, but when one seeks to directly compute acoustic sources, not only the order of the scheme is important, but also the characteristics of propagating waves must be considered [26]. Thomas and Roe [27] argue that an important parameter is the number of mesh points required per wavelength to hold dissipation and dispersion within acceptable bounds. It is suggested by Tam [28] that approximately six to eight grid points per wavelength is required for reasonable wave resolution. Larsson et al [1] investigated these parameters and found that high-resolution grids with less than 1% stretching are required with at least 4 points per wavelength needed to resolve a sound wave. Therefore, the smallest wavelength or highest frequency to be resolved should determine the spatial resolution of the grid. Hence for industry related acoustic problems a large number of grid points are required to obtain correctly resolved waves.

2.4 Computational Aeroacoustics Using Flow-Field/Sound-Field Hybrid Approaches

The fundamental assumption of a one-way coupling between flow and sound is apparent in all acoustic analogies that are based on Lighthill's formulation. Acoustic analogies decouple the propagation of sound waves from their generation, that is, sound is generated by flow inhomogeneities but the flow itself is not influenced by the acoustic field [6]. Therefore, information regarding the near-field flow can be obtained using traditional CFD techniques and this information can then be used to carry out acoustic analysis to predict the propagation of sound to the far-field [29].

This study will consider hybrid turbulence modeling techniques which blends unsteady Reynolds Averaged Navier-Stokes (URANS) with Large Eddy Simulation (LES). This section presents a discussion of different approaches as well as their respective impacts on obtaining acoustical sources. The scalar equations, often called acoustic analogies, were generally derived for the purpose of estimations of the radiated sound from jets or propellers and fans by Lighthill [30]. Methods based on the acoustic analogy require only near-field flow information, providing a cost-effective alternative to resolving the acoustic waves up to the far-field via direct acoustic computation. It has been noted that in industry and academia an acceptable/reasonable method to investigate turbulent structures at high Reynolds number tandem cylinder flows is a large-eddy simulation which will be fundamental to this study.

2.4.1 Computation of Noise Producing Turbulent Structures using DNS or LES With Acoustic Analogy

DNS is mainly used on turbulent flows and attempts to capture the dynamics of all physical scales [31]. In a DNS simulation the range that contains energy and the dissipative range of scales must be resolved. To capture these adequately a fine mesh will be required, this ensures that information regarding small scale statistics is available [21]. Computational issues tend to lead to compromises with DNS simulations, these are required for computational efficiency and stability [31].

In order to predict turbulent flow structures, which are responsible for broadband noise, a DNS or an LES must be performed. This has lead to many computational results for sound generation, being computed using DNS, where all relevant scales of motion are resolved [7]. This approach is computationally expensive however and will require sizeable resources to adequately capture the sound signatures. The resolution of all turbulent length scales must be resolved and hence cannot be fully explored for technically relevant Reynolds numbers [32]. According to Colonius and Lele [21] this approach filters small spatial and high frequency fluctuations from the solution. They highlight that the impact of this type of filtering on sound generation has not yet been characterized in any systematic way.

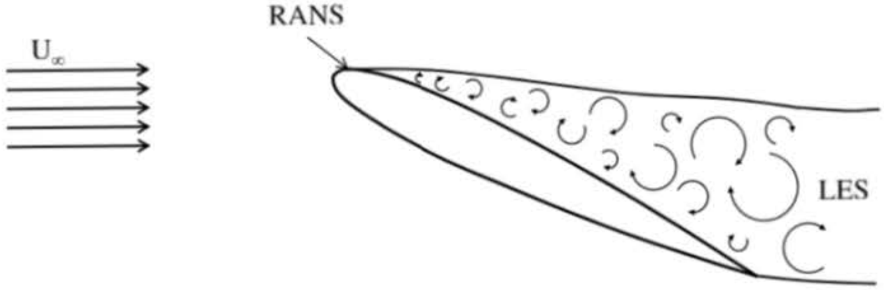

Figure 2: The figure shows how the simulation is configured to implement the global approach of obtaining turbulent fluctuations and subsequent sound sources [5].

2.4.2 RANS/LES Hybrid Approaches With Acoustic Analogy

Flow Field

The most straightforward numerical method is based on solutions of the RANS equations which yield only statistical information of the turbulent flow field and not the unsteady turbulent flow features. Boris et al [33] state that LES is a means to simulate the fluctuating pressure field, however a complete LES of, say, an aircraft wing with deployed flap and slat is still well beyond the capability of todays computing resources. This has lead to considerable interest in hybrid RANS/LES approaches concerning unsteady simulations on local elements i.e. the wake region between cylinders. According to Nebenfuhr et al [5] there are different approaches for RANS/LES modelling, which are hybrid approaches that use different meshes to compute the turbulent fluid flow, acoustic sources and propagation of fluctuating values.

Global Hybrid Approaches

Global approaches combine RANS/LES approaches into a single method. More specifically, the boundary layer of the included geometry is treated in Unsteady Reynolds Averaged Navier-Stokes (URANS) mode, whereas the flow away from the geometry i.e outside the boundary layer is treated in LES mode [5]. The grid resolution requirements for the RANS method on the boundary layer are much more relaxed than for LES, which results in a considerable reduction of the total grid cells required [5]. Figure 2 illustrates how a global hybrid method would be typically set up for a simple aerofoil geometry.

Zonal Hybrid Approaches

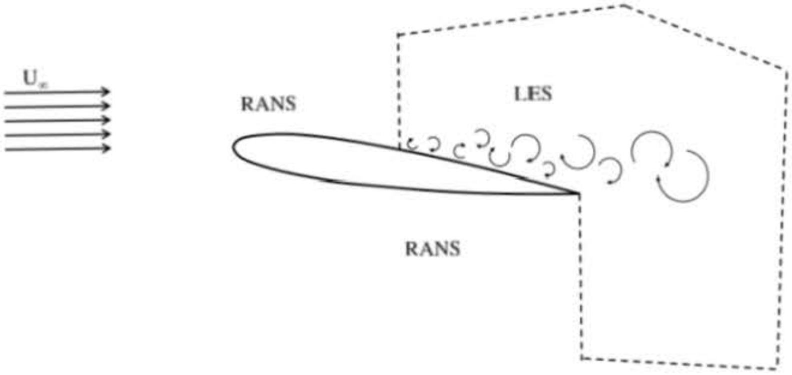

Figure 3: This schematic illustrates a RANS/LES approach that embeds the LES region of interest between the RANS region [5].

Unsteady zonal hybrid RANS/LES simulations have been used by Terracol et al [34] to provide a comprehensive description of the unsteady flow inside the slat cove region of a high-lift device. The focus of their study was to investigate the noise generating physical phenomena within the region using a hybrid URANS/LES approach. Zonal methods isolate user specified regions that are to be treated by U/RANS and LES . This method allows researchers to significantly reduce the cost of an accurate numerical prediction of the unsteady flow around wings compared to a complete LES.

As previously discussed the grid resolution requirements for the RANS method on the included object boundary layer are much more relaxed than for LES, it is also possible to only specify LES in a small region of interest. Hence the LES specified region would be surrounded by the RANS region. These kinds of approaches are known as Embedded LES regions [5] and can prove useful in acquiring sound sources from the region between the cylinders. Figure 3 graphically illustrates the concept on an aerofoil.

Acoustic Field

Due to the computational expense required for DNS, the amount of scales to be resolved must be reduced through an averaging operator, this produces the RANS equations which can be used to resolve scales within the boundary layer [7]. It is noted by Zingg and Godin [35] as well as Tam [28] that in the LES region, the sound field associated with the turbulent flows is available, as long as errors associated with the subgrid scale (SGS) model do not overwhelm the model. Hence this method makes it feasible to compute flows and acoustics at engineering Reynolds numbers.

Cox et al. [36] investigated the vortex shedding noise for cylinders. They used 2-D URANS simulations to generate the flow field. The near-field results were used to predict the far-field acoustic pressure perturbations by solving the Ffowcs-Williams and Hawkings equation. The acoustic results were compared with the experimental results of Revell [37] which showed an over-prediction of the shedding frequency, the peak and overall sound pressure levels. This lead to them concluding that 2-D URANS simulations lead to an over prediction of both noise amplitude and frequency due to spanwise contributions that are neglected in 2-D. It is noted by Konig et al. [32] that unsteady RANS simulation are not ideal for a detailed analysis of the sound generating flow structures. This is because RANS turbulence models do not predict turbulent flow structures, which are responsible for broadband noise [32].

De Villiers [7] showed that LES is efficient at the prediction of aeroacoustic noise sources and it should be noted; that in LES simulations the effect of the subgrid-scale model is not negligible. SGS models interact with the discretisation errors inherent in the numerical scheme which can have a non-trivial impact on the acoustical information predicted [21].

Weinmann et al. [15] investigated the flow and acoustic performance of various hybrid RANS/LES methods including the Spalart Almaras IDDES model. They approximated the flow-field about cylinders in tandem and calculated the far-field noise using a compact form of Curle's analogy. They compared their results to the experimental data of Jenkins et al. [11], [12] and Neuhart et al. [13]. They note that the acoustic spectra predicted show good agreement with experimental results at various microphone positions, with some deficiencies in capturing the broadband noise levels at high Strouhal numbers ($St > 1$).

Souliez et al. [38] performed aerodynamic noise computations from landing gear in a uniform flow using the FW-H equation. The FW-H equation was solved using surface integrals over both the landing gear surface and a permeable surface away from the landing gear. The results for the porous FW-H surface predictions showed good agreement with experiment, whereas the solid FW-H surface predicted pressure fluctuations that were off by some 50% from experimental data. They conclude that quadrupole effects may represent a significant contribution to the overall near-field sound pressure level.

2.4.3 Systems Of Equations With Source Terms

The general idea is to start from the governing equations, and to simplify them for acoustics which typically means that viscosity can be neglected, and that the equations can be linearized [21]. The gain over direct computation is that, since the flow and the acoustics are solved for separately, the computational grids and the numerics can be better suited to what is needed to be resolved between the flow (turbulence) or the acoustics. This typically means much larger cell sizes in the acoustic simulation, hence, much fewer cells [1].

In order to introduce the broadband noise prediction in the industrial design, less computationally intensive procedures should be developed. It has been noted by Ewert and Schröder [39] that LES computations are out of the range for industrial applications especially when numerous configurations have to be studied. They propose and apply a hybrid approach to the analysis of high-lift device slat noise. The first step in their analysis is to determine the flow field by a LES, then the sound field is computed by a numerical solution of a system of acoustic equations referred to as the acoustic perturbation equations (APE) [32], [25].

2.5 Computational Issues: discretisation

There are numerous difficulties associated with numerical methods for problems of sound generation and propagation. These arise due to the nature of acoustic waves, which are very weak compared to near-field fluctuations [21]. The main reason for this according to Colonius and Lele [21] is that they must propagate with minimal attenuation over long distances. In practice this has lead to the use of higher-order-accurate numerical methods, such as compact (Pade), optimized finite difference (FD) and the Fourth-Order Runge-Kutta Method, used for modeling wave propagation.

Dealing with unsteady phenomena requires temporal as well as spatial discretisation. The time domain is divided in time intervals or time steps. A time-marching method is needed to solve the quantities in time. Hence, a semi-discrete system is used to solve the problem [40]. In acoustics, an important phenomenon to consider is numerical dispersion. It is an unphysical phenomenon caused by discretizing the wave equation which makes the waves velocity frequency dependent [26].

This was mitigated by Yang et al [26] using a Fourth-Order Runge-Kutta Method with low numerical dispersion. They noted that the conventional finite-difference (FD) methods for solving the acoustic wave equation often suffer from unwanted numerical dispersion when the grid points per wavelength are too few.

According to Colonius and Lele [21] factors that determine the best choice of method include ease of implementation which includes the ease of imposing of boundary conditions, the efficiency of parallelization, memory requirements and the potential for straight forward implementation on various geometries and flow configurations. The discretisation method considered in this study will be the finite volume approach. According to Colonius et al [21] this approach is attractive because the staggering of fluxes with respect to the conserved variables allows global conservation principles to be enforced discretely. Closely monitoring other sources of error such as reflective boundary conditions and sub-grid scale model is also essential to accurately capturing acoustic wave propagation.

3 Flow and Acoustic Models

The focus of this section will be an analysis of the mathematical tools required for the derivation of Lighthill's analogy and subsequent analogies. He introduced an acoustic analogy, in which the unsteady fluid flow is replaced by a volume distribution of equivalent acoustic sources throughout the entire flow field [22]. Lighthill's theory of aerodynamic noise is the starting point for the understanding and description of acoustic analogies [41].

3.1 Flow Equations

This study will consider sub sonic flows (Mach ≤ 0.3) which corresponds to landing speeds. The governing equations of fluid flow namely conservation of mass and the momentum equation are fundamental in the derivation of the acoustic analogies [30]. The conservation of mass equation is given by:

$$\frac{\partial \rho}{\partial t} + \frac{\partial \rho u_i}{\partial x_i} = 0. \tag{1}$$

Equation (1) is the unsteady, mass conservation or continuity equation at a point in a compressible fluid. The assumptions made are; firstly, the aircraft will approach at subsonic speeds (Mach 0.1274), this implies that the dependency between pressure and density becomes weak and the conservation of mass equation simplifies to:

$$\frac{\partial u_i}{\partial x_i} = 0, \tag{2}$$

and secondly external forces, such as gravity and body forces are absent in the flow field, this results in a simpler form of the Navier-Stokes equations. Therefore the momentum equation is given by:

$$\frac{\partial \rho u_i}{\partial t} + \frac{\partial \rho u_i u_j}{\partial x_j} = -\frac{\partial p}{\partial x_j} + \frac{\partial \tau_{ik}}{\partial x_j}, \tag{3}$$

where ρ, u_i and p respectively denote fluid density, the i^{th} component of the velocity vector and pressure.

The Reynolds stress term τ_{ik} is given by:

$$\tau_{ik} = 2\hat{\mu}_{eff} \left[\frac{1}{2} \left(\frac{\partial u_i}{\partial x_k} + \frac{\partial u_k}{\partial x_j} \right) - \frac{2}{3} \frac{\partial u_j}{\partial x_j} \right]. \tag{4}$$

This relation holds if the fluid is Newtonian and assumes Stokes hypothesis holds. The coefficient $\hat{\mu}_{eff}$ represents the effective eddy viscosity.

3.2 Acoustic Analogies

The derivation of the acoustic analogies relies on the above mass conservation and momentum equations. Lighthills theory of aerodynamic noise and its applications, assume all solid boundaries are absent from the flow field [30]. The adaptation of the theory to include stationary solid surfaces, and the subsequent theory to develop boundary-layer noise was first investigated by Curle [42], subsequently Ffowcs-Williams and Hawkings [43] (FW-H) extended Curles analogy to incorporate the arbitrary motion of solid boundaries.

Larsson et al. [1] modified Curle's analogy in line with the observations made by Sakar and Husseini [44]. This lead to the derivation of a version of Curle's analogy that makes use of strictly time derivatives which is less sensitive to numerical errors. Brentner and Farassat [2] note that it was Ffowcs-Williams himself who proposed to use a permeable data surface to account for nonlinearities in the vicinity of a moving surface. They hence derived a formulation of the FW-H analogy for a permeable surface enclosing the acoustic sources. They showed that this method is advantageous over the original formulation because the costly volume integral, which accounts for the quadrupole sources in the flow, produces negligible contributions. This section will comprise of a discussion on the afore-mentioned modified analogies. Figure 4 depicts the process of numerically obtaining acoustic sources from aerodynamic flows.

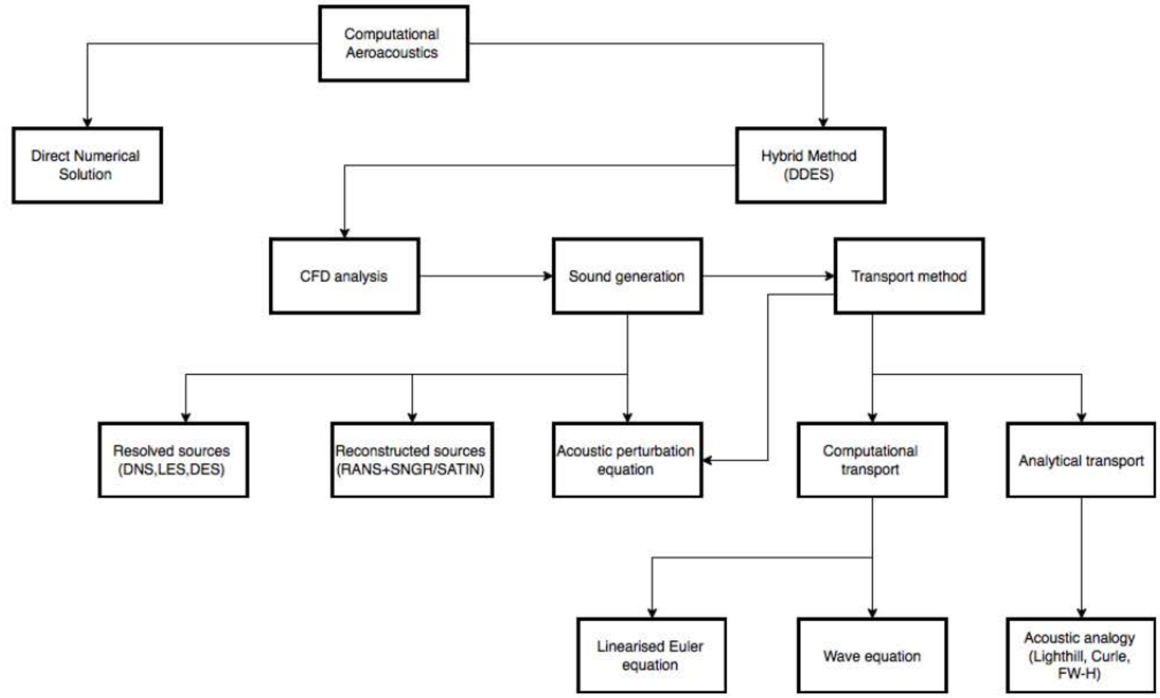

Figure 4: This figure provides a schematic of the algorithmic approach to computational aeroacoustical problems.

3.2.1 Acoustic Quantities

The pressure perturbations $p\prime\left(\mathbf{x},t\right)$ which propagate as waves and are audible to the human ear are now discussed. The perturbations considered (uniform and stagnant/quiescent) allow the conservation laws and constitutive equations to be linearised [41]. The perception of sound is the response to a physical stimulus to the ear known as the unsteady (fluctuating) sound pressure $p\left(\mathbf{x},t\right)$:

$$p\prime\left(\mathbf{x},t\right)=p\left(\mathbf{x},t\right)-p_0. \tag{5}$$

The steady part, which is not audible, p_0 , gives the constant pressure which does not vary in space and time. For harmonic pressure fluctuations the audio range is within the interval 20Hz $\leq$ f $\leq$ 20kHz [41].

3.2.2 Lighthill's Acoustic Analogy for Free Jet Streams

The key idea of Lighthill theory is to derive from the compressible equation of mass (1) and momentum conservation (3), a homogeneous wave equation in a region surrounding the listener. To do this the partial time derivative of the continuity equation is taken and the divergence of (3) is subtracted [29], this yields:

$$\frac{\partial^2 \rho u_i}{\partial t^2} + \frac{\partial^2 \rho u_i u_j}{\partial x_i \partial x_j} = -\frac{\partial^2 p}{\partial x_j^2} + \frac{\partial^2 \tau_{ik}}{\partial x_i \partial x_j}. \tag{6}$$

At this point, the density and pressure fluctuations in a quiescent fluid are considered. This is done by introducing perturbations of both pressure and density:

$$p = p\prime + p_0, \tag{7}$$

$$\rho = \rho\prime + \rho_0. \tag{8}$$

Once the perturbations have been introduced, the term $-c_0 \frac{\partial^2 \rho}{\partial x_i^2}$ is added to both sides. The resulting equation is lighthill's inhomogeneous wave equation for acoustic density fluctuations:

$$\frac{\partial^2 \rho\prime}{\partial t^2} - c_0 \frac{\partial^2 \rho\prime}{\partial x_i^2} = A\left(\mathbf{x}, t\right), \tag{9}$$

where c_0 is the ambient speed of sound and $A(\mathbf{x}, t)$ is the source term, given by

$$A(\mathbf{x}, t) = \frac{\partial^2 T_{ij}}{\partial x_i \partial x_j}. \tag{10}$$

This can be interpreted as the quadrupole acoustic distribution in an ideal atmosphere at rest where T_{ij} is the Lighthill tensor and is defined to be:

$$T_{ij} = \rho u_i u_j + \left(p\prime - c_0 \rho\prime\right) \delta_{ij} - \tau_{ij}. \tag{11}$$

By assuming the wave propagation is isentropic, the relation $p\prime(\mathbf{x}, t) = c_0 \rho\prime(\mathbf{x}, t)$ holds and can be used to generate lighthill's inhomogeneous wave equation for acoustic pressure fluctuations, given by:

$$\frac{1}{c_0}\frac{\partial^2 p\prime}{\partial t^2} - \frac{\partial^2 p\prime}{\partial x_i^2} = A\left(\mathbf{x}, t\right) \tag{12}$$

Lighthill's acoustic analogy was mainly developed for free jet streams. No rigid objects or surfaces are allowed within the computation domain, making this analogy inconvenient due to the large amount of technical application cases (such as this study) that need to take such surfaces into account [45]. This equation is however useful in the study of the numerical properties of the wave equation i.e left hand side of equation (12), as well as to study the required mesh resolution per wavelength in order to reasonably simulate the propagating sound waves from source, with minimal attentunation and dispersion.

3.2.3 Modified Curle's Analogy

Curles acoustic analogy takes rigid and stationary surfaces and objects within the computation domain into account. Now the global sound field is a contribution of the following sources according to Curle's [42] solution to Lighthill's equation:

$$\rho(\mathbf{x}, t) - \rho_0 = \frac{1}{4\pi c_0^2}\frac{\partial^2}{\partial x_i \partial x_j}\int_V \left[\frac{T_{ij}}{r}\right] \mathrm{d}V - \frac{1}{4\pi c_0^2}\frac{\partial}{\partial x_i}\int_S \left[\frac{n_j}{r}\left(p\delta_{ij} - \tau_{ij}\right)\right] \mathrm{d}S, \tag{13}$$

where ρ_0 is a constant of integration, $r = |\mathbf{x} - \mathbf{y}|$ is the distance from the source to the observer, and n_j is the surface normal pointing towards the fluid. The square brackets in the integrands imply they are to be evaluated at the retarded time given by $\tau = t - \frac{r}{c_0}$, defined to be the time at which the source radiation of a fluctuation reaches the observer at t [23].

According Larsson et al. [1], the form of Curle's solution is unideal for numerical computation, as the derivative terms are not in the integrands. It is also noted by Sakar and Husseini [44] that the original form of the equations will need fairly high resolution in time. They argued that it is optimal to rewrite the equations by assuming that r is much larger than the extent of the sources, and to convert the spatial derivatives into temporal ones [44]. The suggested modification, factors these two aspects into a new form of the equation and is thus implemented in the aeroacoustic analysis of the proposed cylinders in tandem.

Consider an arbitrary function of the retarded time $f\left(\tau\right)$. If one wanted to transform its spatial derivative $\frac{\partial f(\tau)}{\partial x_i}$ into temporal ones, the chain rule should be applied as follows:

$$\frac{\partial f\left(\tau\right)}{\partial x_i} = \frac{\partial f\left(\tau\right)}{\partial \tau}\frac{\partial \tau}{\partial x_i} = -\frac{1}{c_0}\frac{\partial r}{\partial x_i}\frac{\partial f\left(\tau\right)}{\partial \tau}. \tag{14}$$

The $\frac{\partial r}{\partial x_i}$ term is given by:

$$\frac{\partial r}{\partial x_i} = \frac{\partial \sqrt{\left(x_j - y_j\right)^2}}{\partial x_i} = \frac{x_j - y_j}{\sqrt{\left(x_j - y_j\right)^2}} = \frac{x_j - y_j}{r} = l_i, \tag{15}$$

where l_i can be interpreted as the unit vector pointing from the source location to the observer location. Using these and the assumption that the observer is where the flow is isentropic, equation (13) can be written as:

$$p\prime(\mathbf{x},t) - p_0 = \frac{1}{4\pi}\frac{\partial}{\partial x_i}\int_V -l_j\left[\frac{\dot{T}_{ij}}{c_0 r} + \frac{T_{ij}}{r^2}\right]\mathrm{d}V - \frac{1}{4\pi}\int_S -l_i n_j\left[\frac{\dot{p}\delta_{ij} - \dot{\tau}_{ij}}{c_0 r} + \frac{p\delta_{ij} - \tau_{ij}}{r^2}\right]\mathrm{d}S. \tag{16}$$

Evaluating the remaining spatial derivative yields:

$$\begin{aligned} p\prime(\mathbf{x},t) - p_0 = \frac{1}{4\pi}\int_V &\left(l_i l_j\left[\frac{\ddot{T}_{ij}}{c_0^2 r} + 2\frac{\dot{T}_{ij}}{c_0 r^2} + 2\frac{T_{ij}}{r^3}\right] - \frac{\partial l_j}{\partial x_i}\left[\frac{\dot{T}_{ij}}{c_0 r} + \frac{T_{ij}}{r^2}\right]\right)\mathrm{d}V \\ &- \frac{1}{4\pi}\int_S -l_i n_j\left[\frac{\dot{p}\delta_{ij} - \dot{\tau}_{ij}}{c_0 r} + \frac{p\delta_{ij} - \tau_{ij}}{r^2}\right]\mathrm{d}S. \end{aligned} \tag{17}$$

The $\frac{\partial l_j}{\partial x_i}$ term in equation (17) is re-expressed as follows:

$$\frac{\partial l_j}{\partial x_i} = \frac{\partial}{\partial x_i}\left[\frac{x_j - y_j}{r}\right] = \frac{\delta_{ij} - l_i l_j}{r}. \tag{18}$$

Substituting this in equation (17) yields the modified Curles analogy proposed by Larsson et al. [1]:

$$\begin{aligned} p\prime(\mathbf{x},t) - p_0 = \frac{1}{4\pi}\int_V &\left[\frac{l_i l_j}{c_0^2 r}\ddot{T}_{ij} + \frac{3 l_i l_j - \delta_{ij}}{c_0 r^2}\dot{T}_{ij} + \frac{3 l_i l_j - \delta_{ij}}{r^3}T_{ij}\right]\mathrm{d}V \\ &+ \frac{1}{4\pi}\int_S l_i n_j\left[\frac{\dot{p}\delta_{ij} - \dot{\tau}_{ij}}{c_0 r} + \frac{p\delta_{ij} - \tau_{ij}}{r^2}\right]\mathrm{d}S. \end{aligned} \tag{19}$$

Sakar and Husseini's form of the volume integral is achieved when r becomes large [44]. The two terms can be interpreted as the sum of the contributions from volume sources (quadropole); which are due to fluctuating stresses in the fluid and surface (dipole) sources which are due to fluctuating forces on the surfaces [1].

3.2.4 Modified Ffowcs-Williams and Hawkings Analogy

Ffowcs-Williams and Hawkings [43] (FW-H) developed an acoustic analogy for solid surfaces moving at an arbitrary speed, v_n. In the original formulation the surface was assumed to be an impermeable geometry. The form of the equation described in [43] to calculate sound generated by turbulence and surfaces in arbitrary motion is given by:

$$\frac{1}{c_0}\frac{\partial^2 p\prime}{\partial t^2} - \frac{\partial p\prime}{\partial x_i^2} = \frac{\partial}{\partial t}\left[\rho_0 v_n \delta\left(f\right)\right] - \frac{\partial}{\partial x_i}\left[p n_i \delta\left(f\right)\right] + \frac{\partial^2}{\partial x_i \partial x_j}\left[H(f) T_{ij}\right], \tag{20}$$

where the Heaviside and the Dirac delta functions are respectively denoted by $H(f)$ and $\delta\left(f\right)$. The moving surface is described by $f(\mathbf{x}, t) = 0$ such that $\frac{\partial f_i}{\partial x_j} = n_i$ where n_i is a component of the outward normal. This implies that $f > 0$ outside the moving surface [2].

The starting point of the modified FW-H is the reformulation of equation (20) to account for a permeable surface enclosure, this is illustrated by figure 5. The philosophy behind using this form is to locate the data surface $f\left(\mathbf{x}, t\right) = 0$ to enclose a moving surface, in such a way that all quadrupoles producing non-negligible noise are included within this surface [6]. This leads to a an acoustic analogy that includes contributions from non-negligible volume sources without the need of calculating a volume integral. The reformulation is given by:

$$\frac{1}{c_0}\frac{\partial^2 p\prime}{\partial t^2} - \frac{\partial p\prime}{\partial x_i^2} = \frac{\partial}{\partial t}\left[\rho_0 U_n\right] \delta\left(f\right) - \frac{\partial}{\partial x_i}\left[L_i \delta\left(f\right)\right] + \frac{\partial^2}{\partial x_i \partial x_j}\left[H(f) T_{ij}\right], \tag{21}$$

where

$$U_n = \left(1 - \frac{\rho}{\rho_0}\right) v_n + \frac{\rho u_n}{\rho_0}, \tag{22}$$

$$L_i = p \delta_{ij} n_j + \rho u_i \left(u_n - v_n\right), \tag{23}$$

Their formula was initially derived for the calculation of rotating blade noise, hence two main sources of sound may be associated to a moving propeller blade. Thickness noise defined to

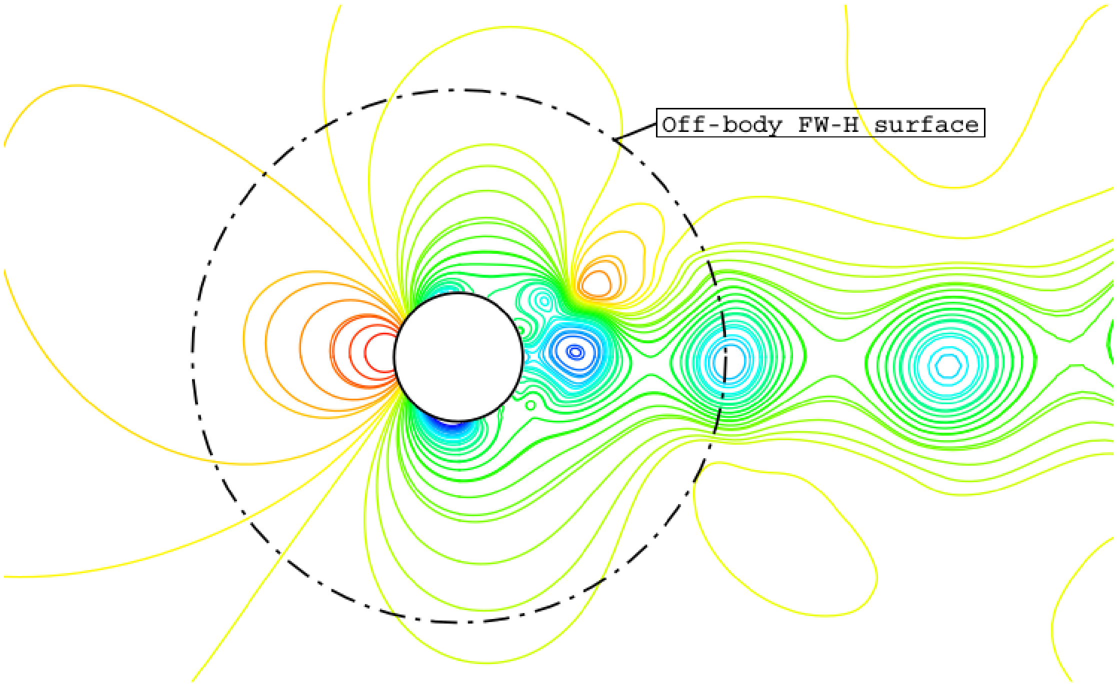

Figure 5: A visual representation from Peers [6] of the permeable surface enclosure used to capture non-negligible volume (quadrupole) sources.

be displacement of fluid by the moving body, and loading noise defined to be the moving lift force distribution [41]. The thickness and loading noise corresponding to Brentner and Farassat [2] formulation 1A are respectively given by:

$$4\pi p'_T\left(\mathbf{x},t\right) = \int\limits_{f=0} \left[\frac{\rho_0 \dot{v}_n}{r\left(1-M_r\right)^2} + \frac{\rho_0 v_n n_i l_i \dot{M}_i}{r\left(1-M_r\right)^3}\right] \mathrm{d}S + \int\limits_{f=0} \left[\frac{\rho_0 c_0 v_n \left(M_r - M^2\right)}{r^2\left(1-M_r\right)^3}\right] \mathrm{d}S, \tag{24}$$

$$\begin{aligned} 4\pi p'_L\left(\mathbf{x},t\right) = &\int\limits_{f=0} \left[\frac{\dot{p} n_i l_i}{c_0 r\left(1-M_r\right)^2} + \frac{\dot{M}_i p n_i l_i l_j}{c_o r\left(1-M_r\right)^3}\right] \mathrm{d}S \\ &+ \int\limits_{f=0} \left[\frac{p\left(n_i l_i - M_i n_i\right)}{r^2\left(1-M_r\right)^2} + \frac{\left(M_r - M^2\right) p n_i l_i}{r^2\left(1-M_r\right)^3}\right] \mathrm{d}S, \end{aligned} \tag{25}$$

Where the near-field and far-field contributions are from the terms of order $1/r^2$ and $1/r$ respectively. M and M_r denote Mach number and Mach number in radiation direction respectively. In this study, the special case of a stationary surface is used, by setting $v_n = 0$.

The total noise emmision from the surface is given by the following relation:

$$p\prime\left(\mathbf{x},t\right) = p\prime_T\left(\mathbf{x},t\right) + p\prime_L\left(\mathbf{x},t\right). \tag{26}$$

3.3 The Spalart-Allmaras IDDES Turbulence Model

Reynolds Averaged Navier-Stokes (RANS) simulations are widely used in industrial CFD, with many RANS turbulence models which have been evaluated for a large variety of flows. Large-Eddy Simulations (LES) resolve the large turbulent scales, the ones smaller than the grid spacing are modelled with a Sub-Grid Scale (SGS) model. According to Menter et al. [46] the starting point for the development of the SST model was the need for the accurate prediction of aeronautics flows with strong adverse pressure gradients and separation. The popular k - ϵ model has been identified to be inefficient in capturing the proper behaviour of turbulent boundary layers up to separation [46].

According to Spalart [47] and Deck et al [48], the Spalart-Allmaras model became quite popular because of its reasonable results for a wide range of flow problems and its numerical properties. It is therefore considered for this study because it provides economical computations of boundary layers up to separation in external aerodynamics. The Spalart-Allmaras model involves one transport equation for kinematic eddy viscosity parameter $\tilde{\nu}$ and a specification of a length scale by means of an algebraic formula [31].

Spalart and Allmaras developed this model for aerodynamic applications, their focus was to remove the incompleteness of algebraic and one equations models based on kinetic energy, and instead, introduce a model that is computationally simpler than two equation models [47]. Their proposed model is a single transport equation for turbulence kinetic viscosity $\tilde{\nu}$.

According to Zingg et al. [35] this model has a proven track record in engineering applications but has shown weakness like other models in predicting boundary layer separation due to adverse pressure gradients. The DES functionality can be implemented for any underlying RANS model, and will be implemented as a modification of the presented original model as presented by Deck et al. [48] and Shur et al. [49]. The one-equation model is given by:

$$\frac{\partial\tilde{\nu}}{\partial t} + u_i\frac{\partial\tilde{\nu}}{\partial x_i} = c_{b1}\left(1 - f_{v2}\right)\tilde{S}\tilde{\nu} - \left(c_{w1}f_w - \frac{c_{b1}f_{v2}}{\kappa^2}\right)\frac{\tilde{\nu}^2}{y} + \frac{1}{\sigma}\left\{\frac{\partial}{\partial x_i}\left[\left(\nu + \tilde{\nu}\right)\right] + c_{b2}\frac{\partial^2\tilde{\nu}}{\partial x_i^2}\right\}, \tag{27}$$

where c_{b1} , c_{b2} , c_{w1} and σ are model constants, y is the distance to the nearest wall and f_w is a wall-damping function. In the production term, $\tilde{S}$ is the vorticity magnitude modified by another the damping function f_{v2} is designed such that correct log-layer behaviour is retained. Another damping function, f_{v1} , is used to obtain the eddy viscosity as $\nu_t = \tilde{\nu}\ f_{v1}$, which now also behaves correctly in the log-layer [48].

The main idea behind DDES implementation is to protect the boundary layer from intrusion by the LES mode and therefore ensuring correct URANS behaviour. To implement this, the y term in the model must be modified by a length scale [49]. This length scale will be based on the grid spacing $\Delta = \max\{\Delta x_1, \Delta x_2, \Delta x_3\}$. The y term is modified as follows:

$$\tilde{y} = y - f_d\ \max\left(0, y - C_{DES}\Delta\right), \tag{28}$$

where

$$f_d = 1 - \tanh\left[(8r_d)^3\right] \quad , \; r_d = \frac{\nu_t + \nu}{\sqrt{u_{i,j}u_{i,j}}\,(\kappa^2 y^2)}, \tag{29}$$

where ν_t and ν repectively denote the eddy viscosity and the molecular viscosity, the expression $u_{i,j}$ denotes the velocity gradients and κ is the von *Kármán* constant and C_{DES} is a constant. The function is designed to be equal 1 in the LES region and 0 elsewhere. This is achieved with the parameter r_d , which is designed to equal 1 in a logarithmic layer and to gradually decrease to 0 at the outer boundary layer edge [48].

So far, the Spalart-Almaras equation with DDES functionality has been discussed. In order to expand this to IDDES another idea in hybrid RANS/LES modeling must be introduced, namely, the use of wall-modeling in LES (WMLES). In WMLES the switch from RANS to LES is performed much closer to the wall, that is, the switch from RANS to LES happens inside the boundary layer, which means that a greater portion of the turbulence is resolved, this is in contrast to traditional D/DES which resolve the boundary in URANS mode. In that sense, the URANS model works as a wall function [5]. A strategy for WMLES, termed Improved DDES (IDDES), has been proposed by Shur et al. [49]; if the inflow conditions contain turbulent content and the grid resolution is fine enough to resolve boundary layer eddies then the IDDES mode will be active. In case these prerequisites are not fulfilled, IDDES will perform as conventional DDES [49].

4 Numerical Implementation

4.1 Open-Source CFD Software OpenFOAM

OpenFOAM is an open source software package for CFD which uses the finite volume approach. The software package is a C++ library that provides two types of applications, solvers and utilities [5]. Solvers are designed to solve problems typically based on continuum mechanics, and utilities perform data manipulation tasks. Due to the open source nature of this software it is possible to add new solvers and utilities or modify the existing ones in order to fit the users requirements [40].

OpenFOAM is widely used in academia and industry as users have access to the source code which allows for greater transparency and reliability. For research the software provides an ideal base to create customised solvers and evaluate different numerical approaches. Lastly, the software permits the user to run large numbers of parallel simulations which is of great benefit if one is interested in costly DES simulations for aeroacoustics. Figure 6 depicts the algorithm for the implementation of the acoustic model on OpenFOAM.

4.2 Finite Volume discretisation

Discretisation of space requires the subdivision of the domain into a number of cells, or control volumes. A set of control volumes (CV) are used for the spatial discretisation. Figure 7 is an example of a control volume where the computational point P is defined in each CV, which is bounded by faces of arbitrary shape. The cells are contiguous, that is, they do not overlap one another and completely fill the domain. A vector **d** is defined, which connects the cell center **N** of the adjacent volume. The face normal area vector for the common face between the cells is denoted by **f**. OpenFOAM defines the majority of its variables such as pressure p and fluid velocity u at P, resulting in a collocated variable arrangement [40].

4.2.1 LES Filtered Navier-Stokes equations

LES approaches filter small spatial and high frequency fluctuations from the solution. The filtering is used to perform a scale separation, which is a locally derived weighted average of the flow properties over a volume of a fluid [7]. An important feature of the filter process is the filter width Δ. The turbulent length scales larger than Δ are retained in the flow field. The

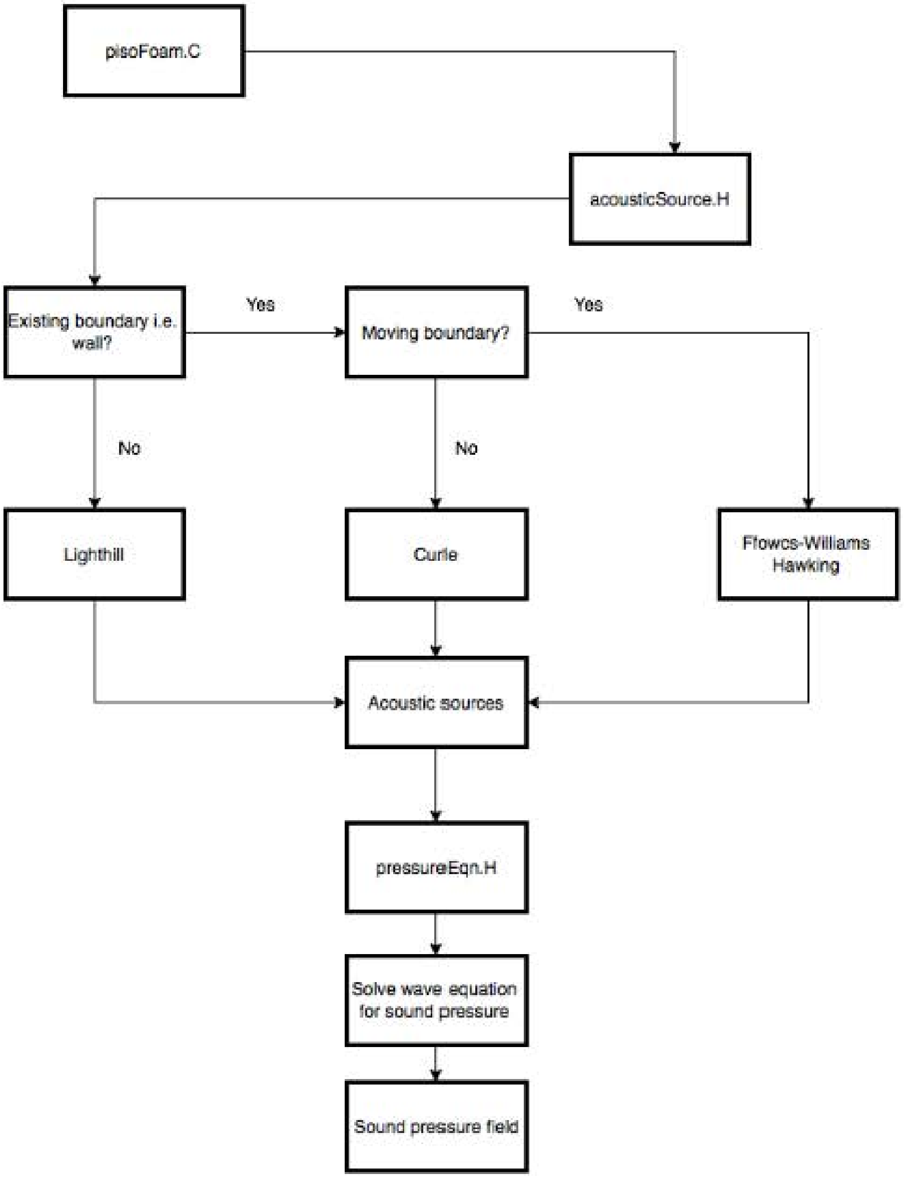

Figure 6: This figure shows a schematic of the algorithm followed for the acoustic solver for incompressible flows.

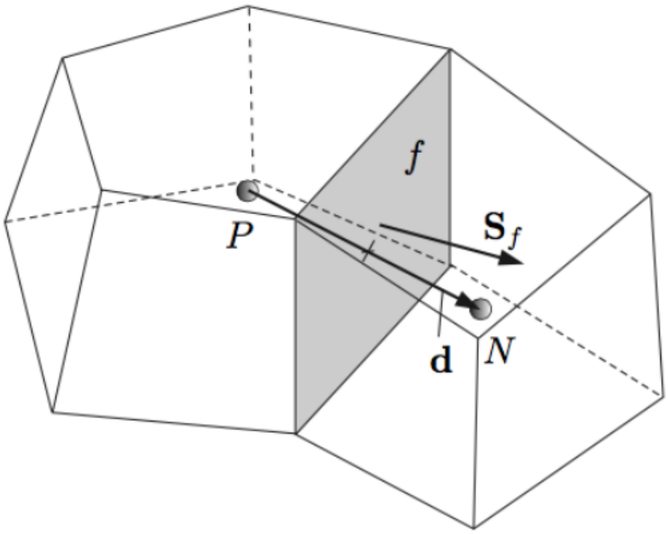

Figure 7: This figure is a schematic of the geometric parameters of the cells in OpenFOAM when the Finite Volume (FV) method is applied as a numerical approach for discretisation.

scales smaller Δ, are modelled using a Sub-Grid Scales (SGS) model [33]. This section forms the starting point of the finite-volume discretisation of LES filtered Navier-Stokes Equations.

Applying the filter to equation (2) and (3) yields the following:

$$\frac{\partial \bar{u}_i}{\partial x_i} = 0, \tag{30}$$

$$\frac{\partial \rho \bar{u}_i}{\partial t} + \frac{\partial \rho \bar{u}_i \bar{u}_j}{\partial x_j} = -\frac{\partial \bar{p}}{\partial x_j} + \frac{\partial \tau_{ik}^R}{\partial x_j} + \nu \frac{\partial^2 \bar{u}_i}{\partial x_j^2}. \tag{31}$$

The non-linear convection term in equation (31) causes a dependency between the resolved and unresolved scales the influence of the unresolved scales must be incorporated in the subgrid-stress tensor. It is given by:

$$\tau_{ik}^R = \rho \left(u_i \bar{u}_j - \bar{u}_i \bar{u}_j \right). \tag{32}$$

An Eddy-viscosity model is used to define the unresolved scales in LES. Therefore, the stress tensor can be written as:

$$\tau_{ik}^{R} = 2\rho\nu_t \bar{S}_{ij} + \frac{1}{3}\delta_{ij}\tau_{kk}. \tag{33}$$

The turbulent viscosity is given by ν_t and when (33) is substituted into (31) the following is yielded:

$$\frac{\partial \rho \bar{u}_i}{\partial t} + \frac{\partial \rho \bar{u}_i \bar{u}_j}{\partial x_j} = -\frac{\partial \bar{p}}{\partial x_j} + 2\frac{\partial}{\partial x_j}\left[\left(\nu + \nu_t\right)\bar{S}_{ij}\right]. \tag{34}$$

Casting equation (30) and (34) into weak form yields:

$$\int_V \frac{\partial \bar{u}_i}{\partial x_i}\mathrm{d}V = \int_S \mathrm{d}A \cdot \bar{u}_i = 0, \tag{35}$$

$$\int\limits_{t}^{t+\Delta t}\left[\frac{\mathrm{d}}{\mathrm{d}t}\int_V \rho\bar{u}_i\mathrm{d}V + \int_V \frac{\partial \rho\bar{u}_i\bar{u}_j}{\partial x_j}\mathrm{d}V\right]\mathrm{d}t = \int\limits_{t}^{t+\Delta t}\left[-\int_V \frac{\partial \bar{p}}{\partial x_j} + \int_V \frac{\partial \hat{\nu}_{eff}}{\partial x_j}\left(\frac{\partial \bar{u}_i}{\partial x_i} + \frac{\bar{u}_j}{\partial x_i}\right)\mathrm{d}V\right]\mathrm{d}t. \tag{36}$$

Equation (36) is a second order equation due to the diffusion term. To obtain good accuracy the discretisation method should yield a second or higher order of accuracy. The temporal term is also second order and hence the temporal discretisation should also to be second or higher order accurate [50].

4.2.2 Spatial discretisation

A summary of the evaluations of integrals on a control volume is now presented. For full derivations please refer to Jasak [51] and de Villiers [7].

Let ϕ be a transported quantity/scalar, which is assumed to vary linearly about the spatial point, $\mathbf{P}$ and time t, as described in figure 8.

Volume integral

$$\int_{V_P} \phi(x)\mathrm{d}V \approx \phi_p V_P, \tag{37}$$

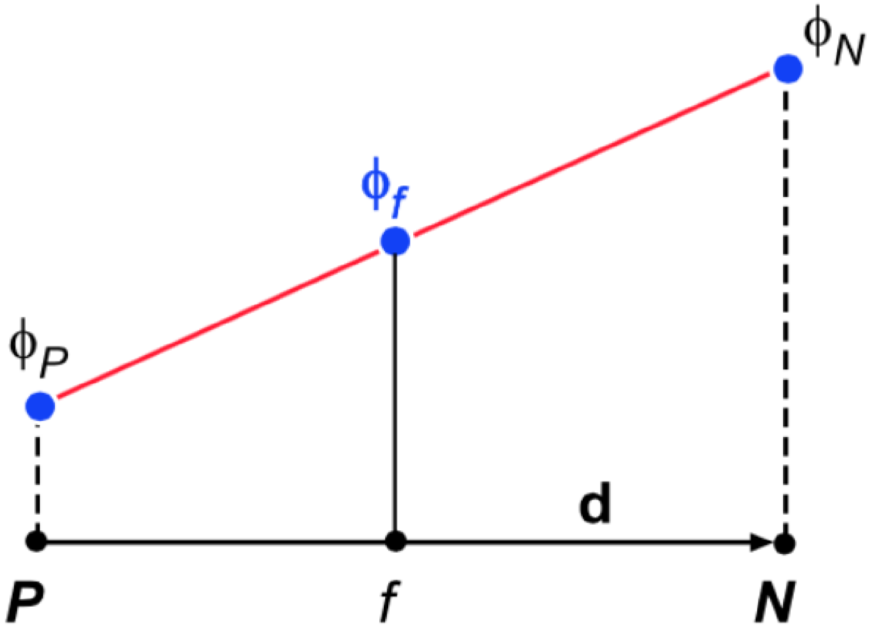

Figure 8: Since linear variation of the dependent variable is assumed, the face centred value ϕ_f can be found from a simple interpolation between the cell values at **P** and **N** [7].

Surface Integral

$$\int_f \phi \mathrm{d}\mathbf{A} = \phi_f \mathbf{A}_f, \tag{38}$$

Integral of divergence

$$\int_{V_P} \frac{\partial \phi_i}{\partial x_i} \mathrm{d}\mathbf{A} \approx \sum_f \mathbf{A}_f \cdot \phi_f, \tag{39}$$

Integral of gradient

$$\int_{V_P} \frac{\partial \phi_i}{\partial x_j} \mathrm{d}\mathbf{A} \approx \sum_f \mathbf{A}_f \phi_f. \tag{40}$$

Convection Term

The convection term is discretized as follows:

$$\int_{V_P} \frac{\partial}{\partial x_j} \left(\bar{u}_j \phi_j\right) \mathrm{d}V = \sum_f \mathbf{A} \cdot \left(\bar{u}\phi\right)_f = \sum_f \left(\mathbf{A} \cdot \bar{u}\right) \phi_f = \sum_f F \phi_f, \tag{41}$$

where F = $(\mathbf{A} \cdot \bar{u})$ represents the the volume flux through the face.

Diffusion Term

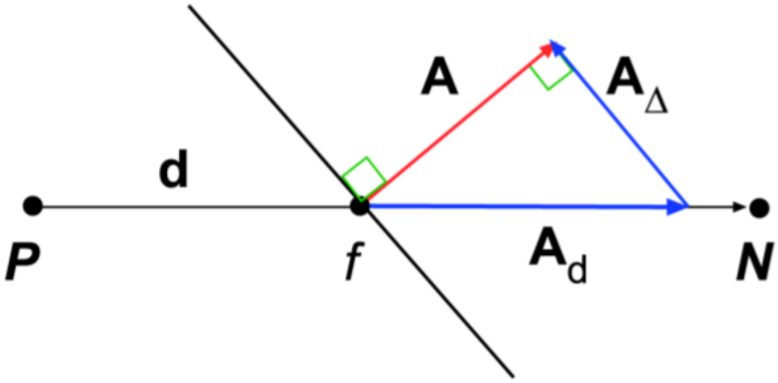

Figure 9: Decomposition of a non-orthogonal cell as illustrated by de Villiers [7].

$$\int_{V_P} \frac{\partial}{\partial x_j}\left(\hat{\nu}_{eff}\frac{\partial \phi_i}{\partial x_j}\right)\mathrm{d}V = \sum_f \mathbf{A}\cdot\left(\hat{\nu}_{eff}\frac{\partial \phi_i}{\partial x_j}\right)_f = \sum_f \hat{\nu}_{eff}\mathbf{A}\cdot\left(\frac{\partial \phi_i}{\partial x_j}\right)_f . \tag{42}$$

The $\mathbf{A}\cdot\left(\frac{\partial \phi_i}{\partial x_j}\right)_f$ term is mesh dependent and will be elaborated on now. For an orthogonal mesh, the face gradient of ϕ can be expressed as follows:

$$\mathbf{A}\cdot\left(\frac{\partial \phi_i}{\partial x_j}\right)_P = |A|\frac{\phi_N - \phi_P}{|d|}. \tag{43}$$

where N denotes the cell neighbouring P . When the mesh is non-orthogonal, the second order accuracy of the scheme ceases to hold when applying equation (43) to the discretisation. An additional term must be introduced that factors in non-orthogonality, figure 9 illustrates geomoetrically, how the additional term is derived. The additional term is given by:

$$\mathbf{A}\cdot\left(\frac{\partial \phi_i}{\partial x_j}\right)_P = |A|\frac{\phi_N - \phi_P}{|d|} + \mathbf{A}_\Delta\cdot\left(\frac{\partial \tilde{\phi}_i}{\partial x_j}\right)_f . \tag{44}$$

If non-orthogonality is high, the correction can result in a negative coefficient which could introduce instability. For LES this is important to factor in and should be considered when structuring a mesh.

4.2.3 Temporal Discretisation

There are various ways to perform a temporal discretisation, however due to the second order accuracy requirement due to the diffusion term, it's essential to ensure that each term in the transport equation be second order accurate [50] [31]. The second order backward differencing scheme is now presented.

Second order Backward Differencing

$$\frac{\partial \phi}{\partial t} = \frac{\frac{3}{2}\phi^{n+1} + \phi^{n} + \frac{1}{2}\phi^{n-1}}{\Delta t}. \tag{45}$$

The truncation error should be minimized throughout the simulation. However, small variations in face fluxes and derivatives can cause errors. These errors can be considered diffusive in nature, which could have a negative impact on the LES mode of the hybrid simulations [40]. To maintain stability throughout the simulation, the cell face Courant number, defined by CFL $= \frac{\bar{\mathbf{u}}_f \cdot \mathbf{n}}{|\mathbf{d}|}$ should be kept below 1 [31]. For all cases presented in this study, the Courant number was kept below 0.5.

4.2.4 Pressure-Velocity Coupling

The PISO (Pressure Implicit with Splitting of Operators) algorithm proposed by Issa [52] is employed to couple the pressure to the velocity. Using the discretisation techniques discussed in the previous section the pressure equation is derived in a semi-discretised form of the momentum equation . To couple these quantities a pressure equation is used and is given by:

$$a_p \hat{u}_p = \mathbf{H}(\hat{u}) - \frac{\partial p_i}{\partial x_j}. \tag{46}$$

The **H** vector is a combination of all the neighbour matrix coefficients multiplied with their velocities and all the non-linear source terms excluding the pressure gradient, but including the current time contributions [7]. The final form of the Navier-Stokes system solved by the PISO algorithm is given by:

$$a_p \hat{u}_p = \mathbf{H} - \sum_f \mathbf{A} \cdot \hat{p}_f, \tag{47}$$

$$\sum_f \mathbf{A} \cdot \left(\frac{1}{a_p}\right)_f \left(\frac{\partial p_i}{\partial x_j}\right)_f = \sum_f \mathbf{A} \cdot \left(\frac{\mathbf{H}}{a_p}\right)_f . \tag{48}$$

5 Results

This chapter presents a verification and validatation of the implemented aeroacoustic model. An open cavity geometry is used as a preliminary validation and verification of OpenFOAM by comparing the acoustic analogy results to that of Parkhi [8]. The applied IDDES turbulence model is verified and validated by assessing its ability to model the incoming boundary layer. This has an impact on the broadband noise producing turbulent structures and is thus regarded as important. The tandem cylinder results follow. The averaging, statistical convergence, hydrodynamic field as well as the acoustic results are presented and compared to experimental data.

5.1 Cavity

For every numerical CFD software package, it is inevitable to verify the CFD code. In a code verification it is required to perform some procedures to identify code mistakes that can affect the simulation. This is done by comparing the results obtained using a CFD code, to the results of obtained by other practitioners. An open cavity case is considered for verification of the turbulence model as well as the acoustic analogies. The turbulence model is verified using the NASA Langley Research Center (LaRC) Turbulence Modeling Resource (TMR) test case. Figure 10 illustrates the flow structure for the cavity case.

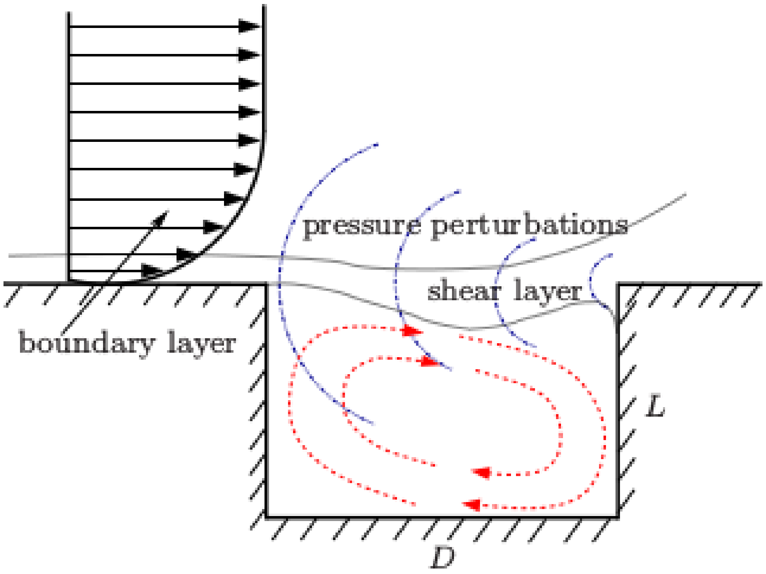

Figure 10: Schematic diagram from Parkhi [8] of the flow structure of a open cavity

5.1.1 Incoming Boundary Layer

Boundary layers are thin regions in the flow where viscous forces are important [53]. The presence of a wall has a non-negligible effect on the processes that produce turbulence [54]. The fundamental assumptions are that the layer is thin in the direction across the streamlines, viscous stresses are non negligible only within the layer and the velocity satisfies the no-slip condition at the wall [53].

Momentum Thickness

The momentum thickness θ, is a theoretical length scale to quantify the effects of fluid viscosity in the vicinity of a physical boundary [53]. Physically it can be interpreted as the distance by which the boundary should be displaced to compensate for the reduction in momentum of the flowing fluid on account of boundary layer formation [53]. It is given by:

$$\theta \equiv \int_0^\infty \frac{\rho}{\rho_\infty} \frac{u}{U_\infty} \left(1 - \frac{u}{U_\infty}\right) \mathrm{d}y \tag{49}$$

The momentum thickness Reynolds number is defined to be:

$$Re_\theta = \frac{\rho_\infty U_\infty \theta}{\mu_\infty} \tag{50}$$

According to de Graff et al. [55] since the viscous length scale decreases rapidly with Reynolds number, the inner and outer scales become increasingly incomparable with increasing Reynolds number. At a momentum thickness Reynolds number $Re_\theta \approx 6000$, the the region below $y^+ \approx 100$ occupies only about 4 % of the total boundary layer thickness and accounts for a large fraction of the total turbulence production. However, at a much higher Reynolds number thickness of, say, $Re_\theta \approx 20000$, the region below $y^+ \approx 100$ occupies only about 1.5 % of the boundary layer thickness, and accounts for only a small fraction of the total turbulence production [55].

5.1.2 Mesh

The case considered in the study has a length to depth ratio L/D = 2 hence according to Pancham [56], is classified as an open cavity. For open cavities a mixing layer is formed at the top corner of the cavity leading edge that impinges with the top corner of the cavity trailing edge. This occurs for length to depth ratios between 1 < L / D < 9.

Required First Cell Height

The following section outlines how the required first cell height was calculated in order to fully resolve the incoming boundary layer. The case was run at incompressible conditions i.e Mach = 0.2. For the grids given below, running at a Reynolds number per unit length of Re = 5×10^5 is sufficient to achieve desired Re_θ levels.

Since $Re < 10^9$ the Shlichting skin-friction correlation is applicable hence:

$$C_f = (2\log_{10}(Re - 0.65))^{-2.3} \tag{51}$$

$$\tau_w = 0.5 \times C_f \times \rho \times u^2 \tag{52}$$

$$u_\tau = \sqrt{0.5 \times C_f \times u^2} \tag{53}$$

Where τ_w and u_τ respectively denote the wall shear stress and friction velocity.

Hence the required cell height to resolve the boundary layer is given by:

$$y = \frac{(y^+) \times \nu}{u_\tau} = 5.592921 \times 10^{-6} \tag{54}$$

Where y^+ is the nondimensional wall-normal distance, which is required to be less than one.

Modelled Cell Height

When a nonuniform mesh grading is used, OpenFOAM calculates the cell sizes using a geometric progression. Along a length L, if n cells are requested with a ratio of R between the last and first cells, the size of the smallest cell, δy , is given by:

$$\delta y = L\frac{r - 1}{\alpha r - 1} \tag{55}$$

where $r = R^{\frac{1}{n-1}}$ and

$$\alpha = \begin{cases} R & R > 1 \\ 1 - r^{-n} + r^{-1} & R < 1 \end{cases} \tag{56}$$

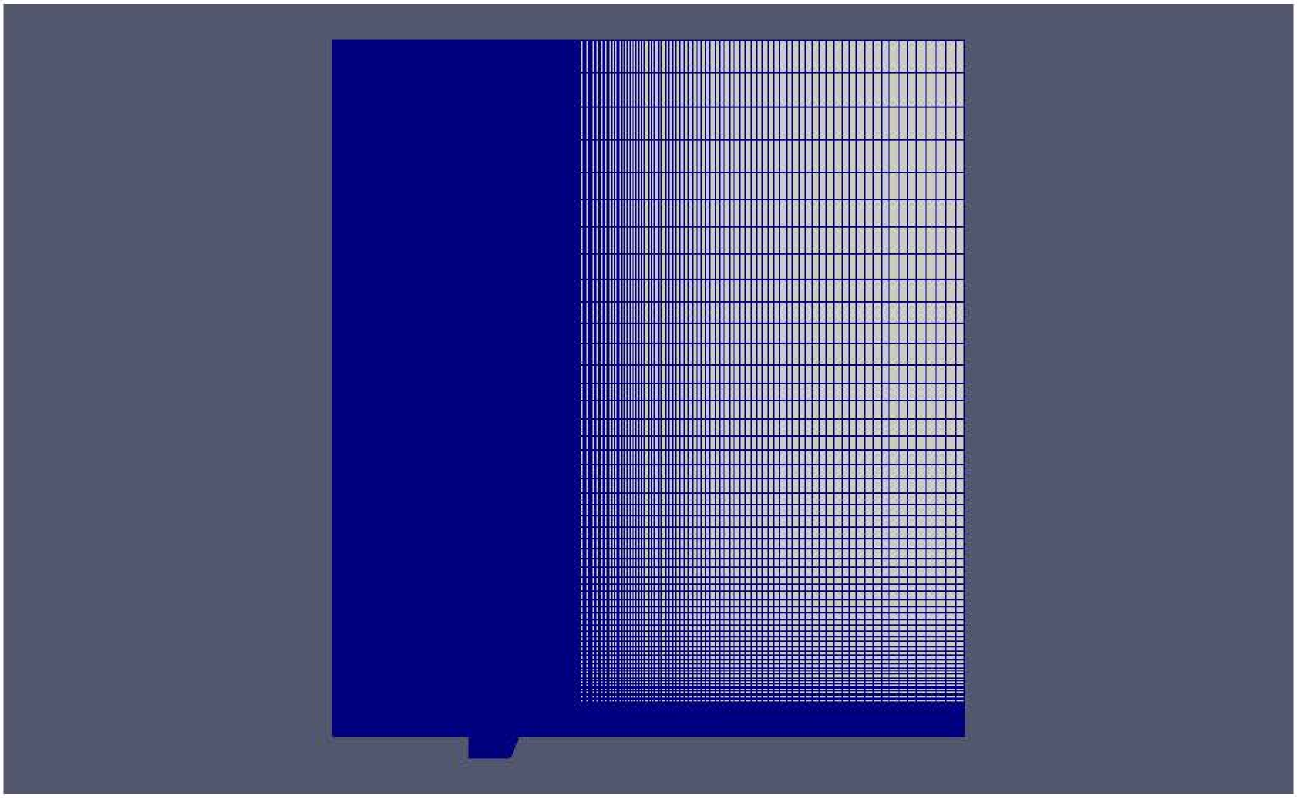

Figure 11: A nonuniform mesh grading was used, this was done to increase mesh resolution near the wall regions in order to capture the vortex generating wall boundary layers.

Using the above formulae yields a modelled first cell height of:

$$\delta y = 5.7998 \times 10^{-7} \tag{57}$$

Hence the implemented mesh has a first cell height that can resolve the boundary layer from the viscous sublayer to the defect layer regions. Figure 12 is a snapshot of the non-uniform mesh used in the cavity case. Figure 13 demonstrates the log law of wall as presented by McDonough [54]. Figure 14 shows the how the modelled results compare againsts NASA's Langley Research Centre (LaRC) Spalart Almaras results at a momentum thickness Reynolds number of $Re_\theta \approx 10000$. An analytical solution proposed by Coles in [9] and [10] is also included. For consistency with the results from LaRC, a $\log_{10}$ scale is applied to the x-axis.

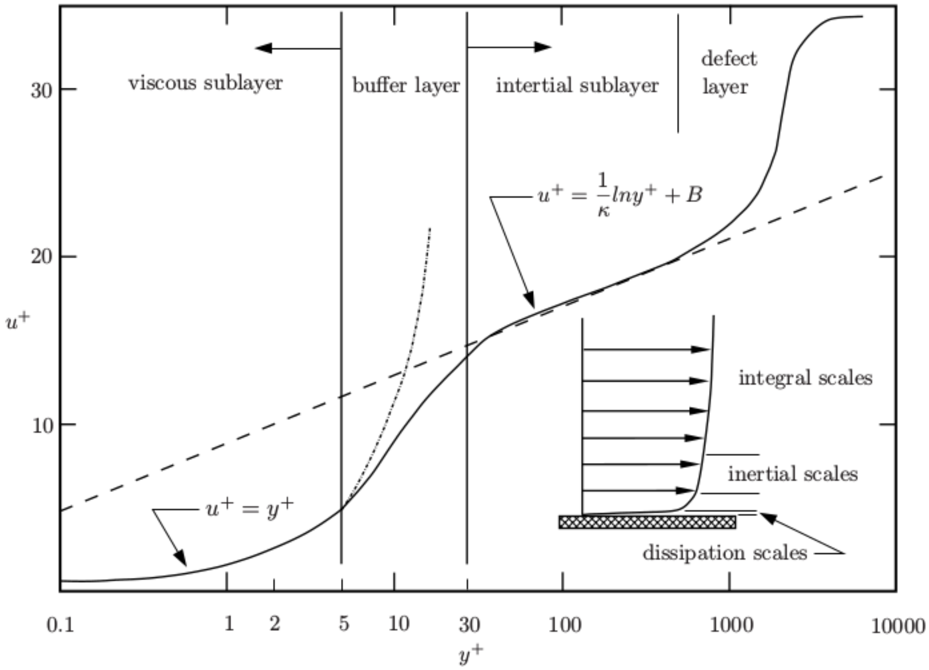

(a) Log law of wall as presented by McDonough [54].

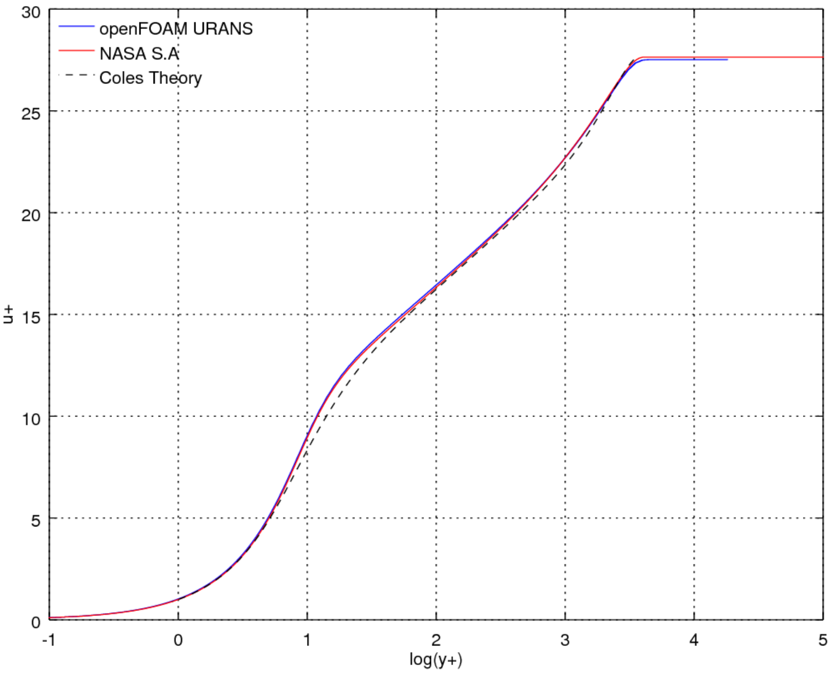

(b) Modelled boundary layer at $Re_\theta = 10000$.

Figure 12: Modelled boundary layer with comparison to LaRC's S.A. solution and Coles [9], [10] solution at a momentum thickness Reynolds number of $Re_\theta \approx 10000$

5.1.3 Acoustic results

Sound Pressure Level

The Sound Pressure Level (SPL), measured in decibels (dB) is given by:

$$SPL = 20 \log \left(\frac{p\prime_{rms}}{p_{ref}} \right) \tag{58}$$

where rms denotes the root mean square, given by: $p\prime_{rms} = \sqrt{(\bar{p}\prime)^2}$. For sound propagating in gasses the reference pressure $p_{ref} = 2 \times 10^{-5}$ Pa is recommended [41]. In practice the threshold of hearing is considered to be at 1kHz, that is, around SPL = 0 dB. In order to detect 1kHz the signal can be integrated over approximately 0.5ms [12]. The maximum sensitivity of the ear is around 3 kHz (pitch of a police man whistle). The SPL for approaching and landing has been found to range between 95 and 120 decibels(dB) respectively. Figure 13 presents a verification and validation of the of modified acoustic analogies. There is good agreement to Parkhi's [8] Curle analogy about the main tone and overall broadband levels correspond well to the experimental data as well as Parkhi's. The modified Curle's analogy has performed much better than the FW-H with respect to capturing experimental data. The modified FW-H over-estimated the overall power spectral density levels for this case.

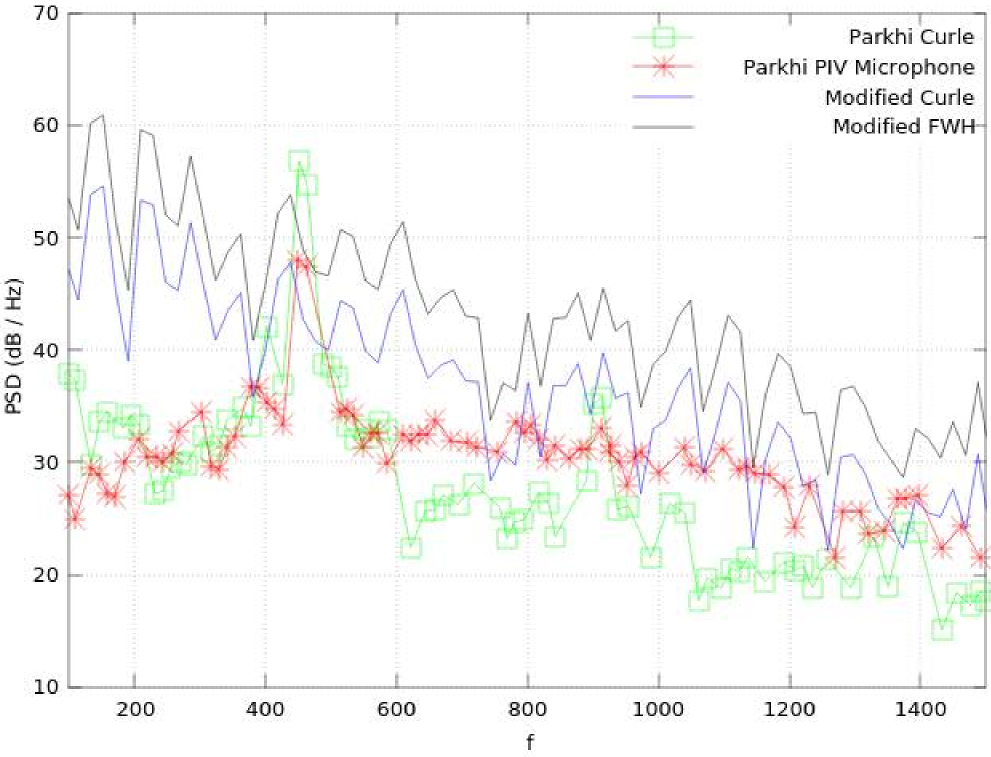

Figure 13: Simulated acoustic results with $\Delta f \approx 19$ compared to those coressponding to Parkhi's [8] Curle analogy. Included are Microphone 13 results for the PIV simulation

5.2 Tandem Cylinders

Flows about tandem cylinders are classed as a problem of wake interference and the distance between the cylinder centres sets the type of wake interaction summarized by figure 14 and table 1 [17].

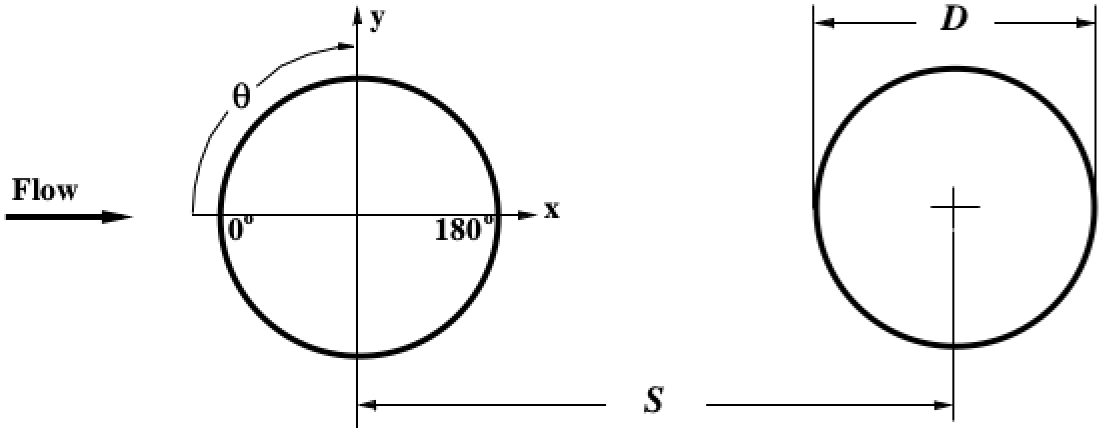

Figure 14: This is a schematic of the proposed cyliders in tandem with $D = 0.05715m$ and $S/D = 3.7$ [6]

Table 1: Approximation of tandem cylinder regimes relative to the ratio S/D [6].

S/D	**Flow Regime**
1.0 - 1.3	Non-reattachment of free shear layers separated from up-stream cylinder on downstream cylinder. Vortex street behind downstream cylinder is formed by the free shear layers from upstream cylinder.
1.3 - 3.3	Free shear layers from upstream cylinder may reattach alternatively, permanently or intermittently onto the downstream cylinder. No shedding in gap region.
3.3 - 4.0	Intermittent shedding behind upstream cylinder. The case in this study considers an S/D ratio of 3.7
4.0 - 6.0	Pairing of eddies from the upstream and downstream cylinders. Synchronisation of the two vortex streets in phase and frequency.
>6.0	Uncoupled vortex shedding behind both cylinders.

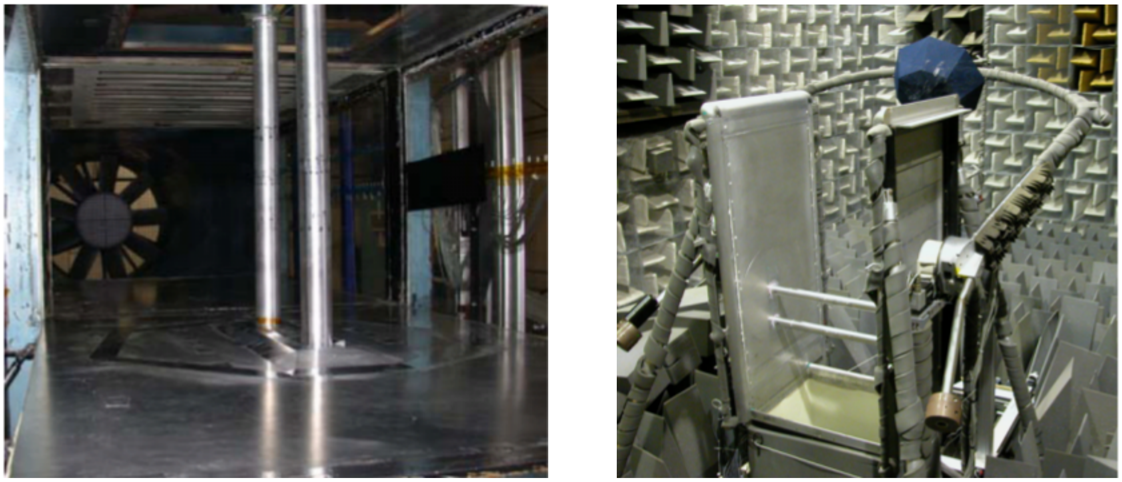

(a) Basic Aerodynamic Research Tunnel (BART)

(b) Quiet Flow Facility(QFF)

Figure 15: Tandem cylinder experimental setup in the Basic Aerodynamic Research Tunnel and Quiet Flow Facility. Photographs from Jenkins et al. [11], [12] and Neuhart et al. [13].

This section includes a comparison of the two modified versions of Curle's and FW-H analogies with experimental data. The results of this study have been benchmarked against NASA's experimental (and numerical) results performed at high Reynolds number (1.66×10^5) by Jenkins et al. [11] [12] and Neuhart et al. [13]. It provides one of the most comprehensive data sets available for aeroacoustic simulation validation. Figure 15 shows the experimental setup for the data used to validate the aeroacoustic model. The BART is a subsonic, atmospheric wind tunnel used to investigate the fundamental characteristics of complex flow fields (figure 15(a)). The tunnel has a closed test section with a height of 0.711 m, a width of 1.016 m and a length of 3.048 m. The experimental free stream velocity was set to 44 m/s to achieve a Reynolds number (using cylinder diameter as characteristic length) of 1.66×10^5. The Quiet Flow Facility (QFF) is NASA's LaRC anechoic wind tunnel (figure 15(b)). The cylinders spanned the 0.914 m section to yield a spanwise aspect ratio of $z/D = 16$.

5.2.1 Mesh

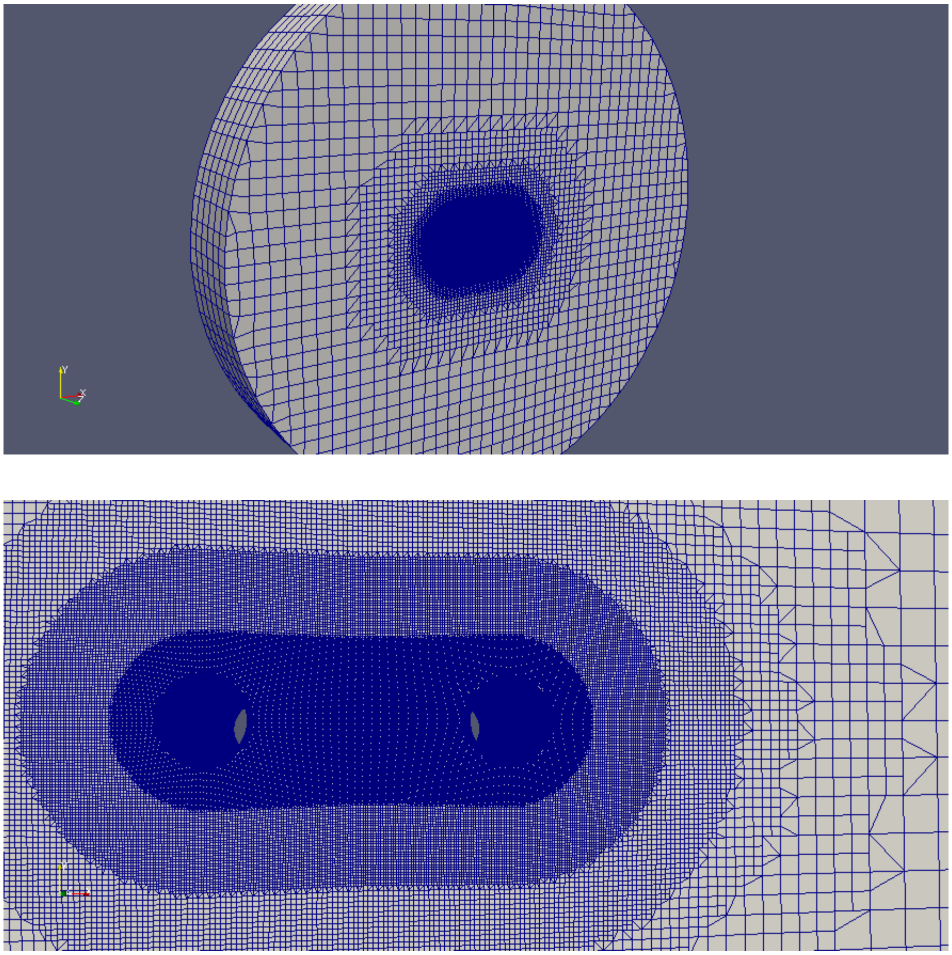

Figure 16: The high resolution computational grid.

In order to fully capture variation in the spanwise direction a domain that extends to $z/D \approx 12$ would be required [18]. The spanwise extent of the cylinders is $z/D \approx 6$. It is noted that there is essential three-dimensional features of the flow that could be missed by setting the simulation up this. As previously stated, the aeroacoustic noise for subsonic velocities is generated due to the turbulent structures interacting with the solid boundaries. To capture the most important effects, a high wall resolution is required as shown in figure 16. Therefore each cylinder was designed to ensure an average first wall-normal grid spacing below 1 i.e. $y^+ < 1$. The total cell count in the domain is roughly 2×10^7 cells.

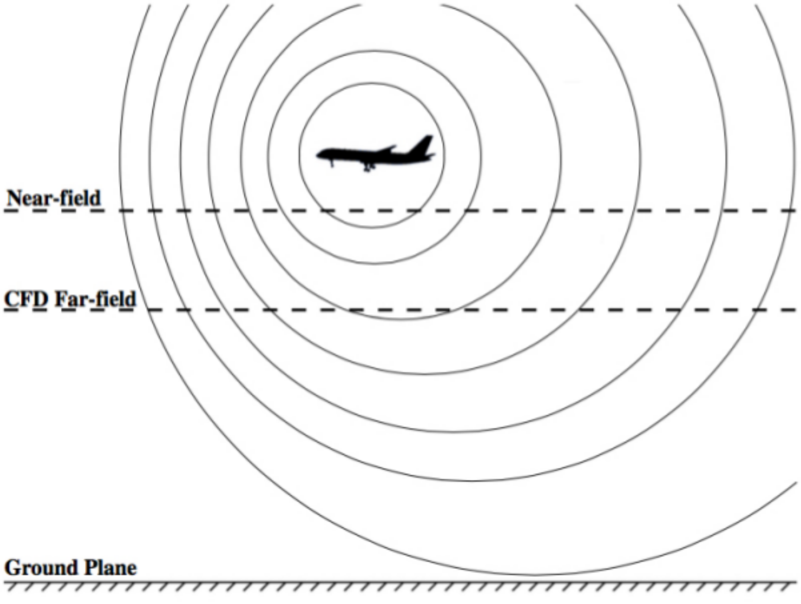

(a) This depicts an industry approach to curb computational issues while capturing the important information from the model.

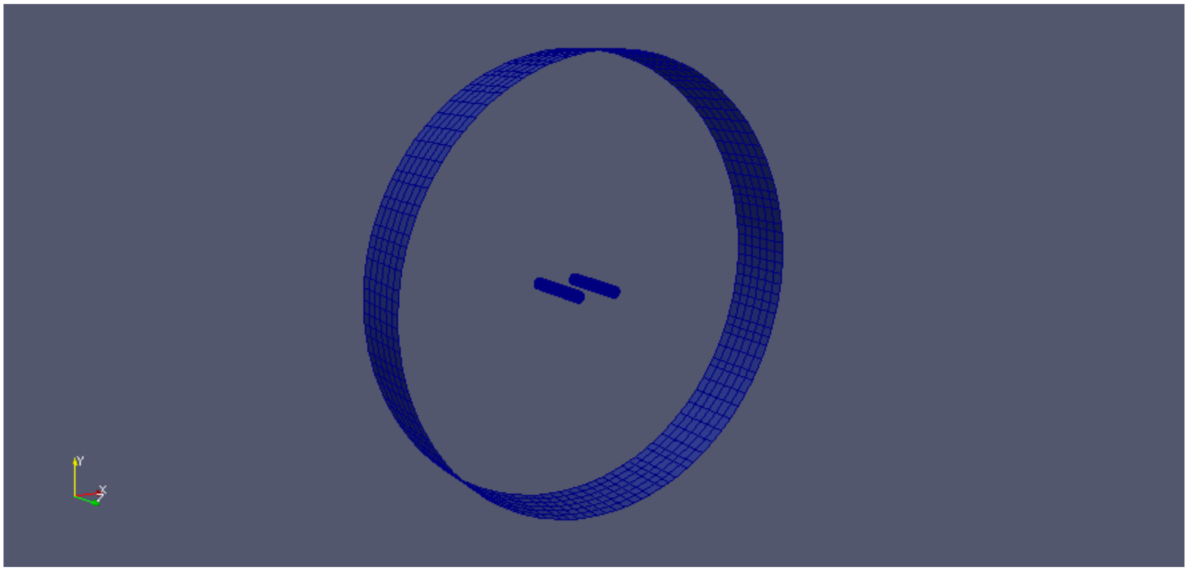

(b) This is an illustration of the cylinders in tandem. It is enclosed by the far-field used for this study. The computational domain consists of a three-dimensional tandem cylinder geomentry with a spanwise extend of $z/D = 6$.

Figure 17: A typical approach to tackle noise problems is to represent the CFD solution on a reasonable computational mesh that does not extend too far from the bodies as shown in the figure [14].

5.2.2 Averaging and Statistical Convergence

A history of lift and drag coefficient predicted by Weinmann et al. [15] is shown in figure 18. Regular vortex shedding from the upstream cylinder is disrupted at $\Delta t U_0/D \approx 600$, this subsequently lead to a strong reduction of fluctuations in the lift and drag coefficient [15]. The modelled history of lift and drag coefficient is shown in figure 19. Over the entire averaging period this anomaly was not captured.

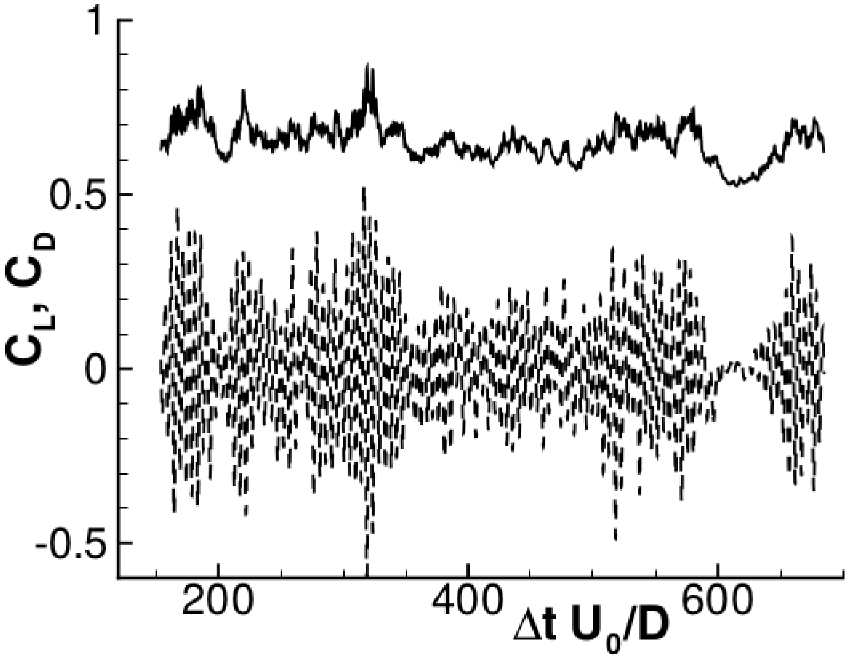

(a) Upstream cylinder

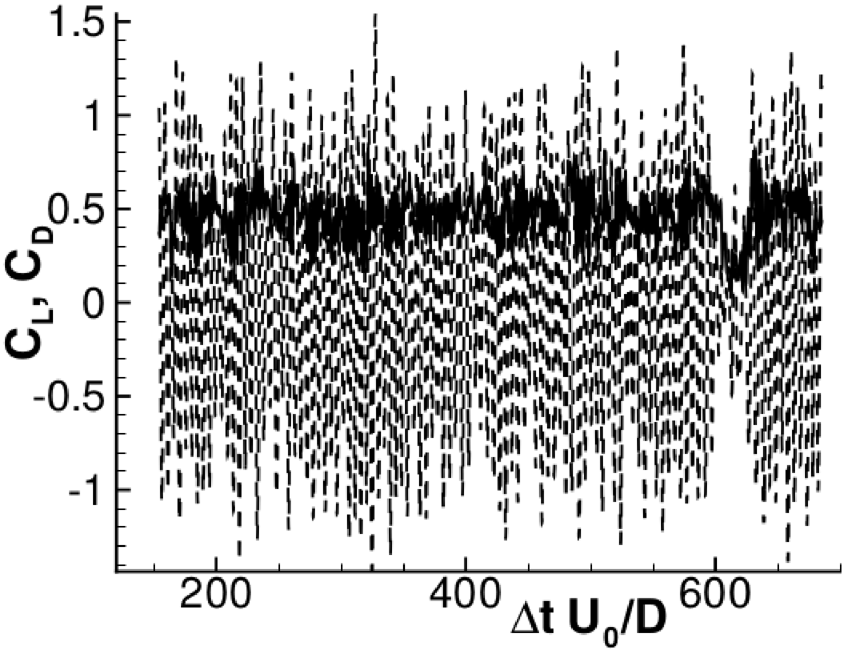

(b) Downstream Cylinder

Figure 18: Histories of the lift and drag coefficients of the cylinders from Weinemann et al. [15]

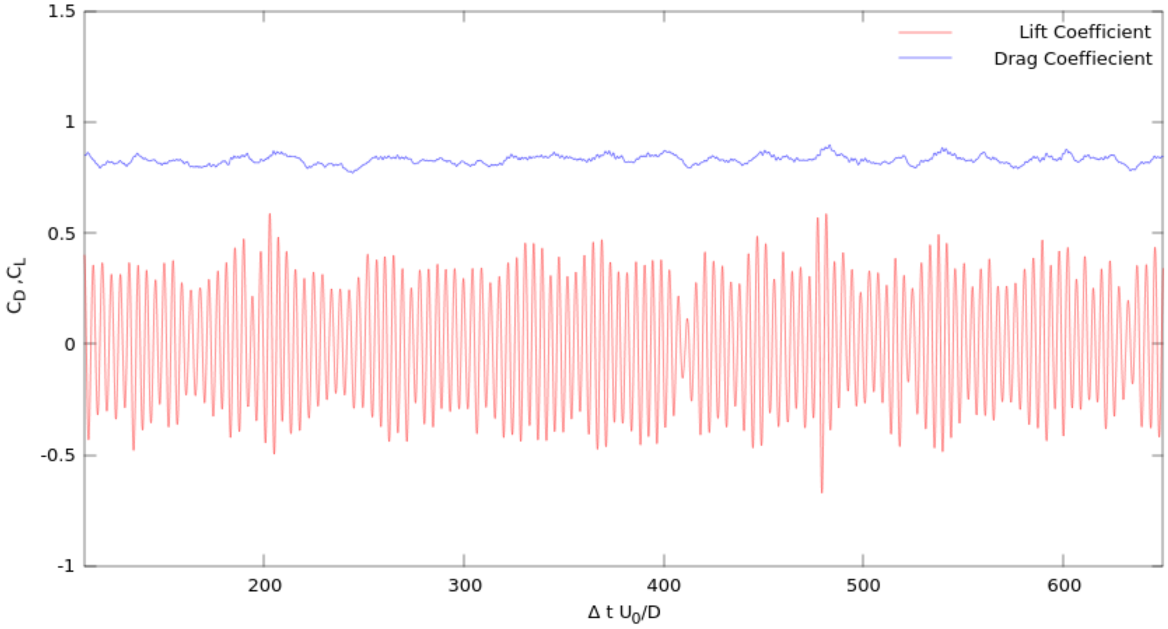

(a) Upstream cylinder

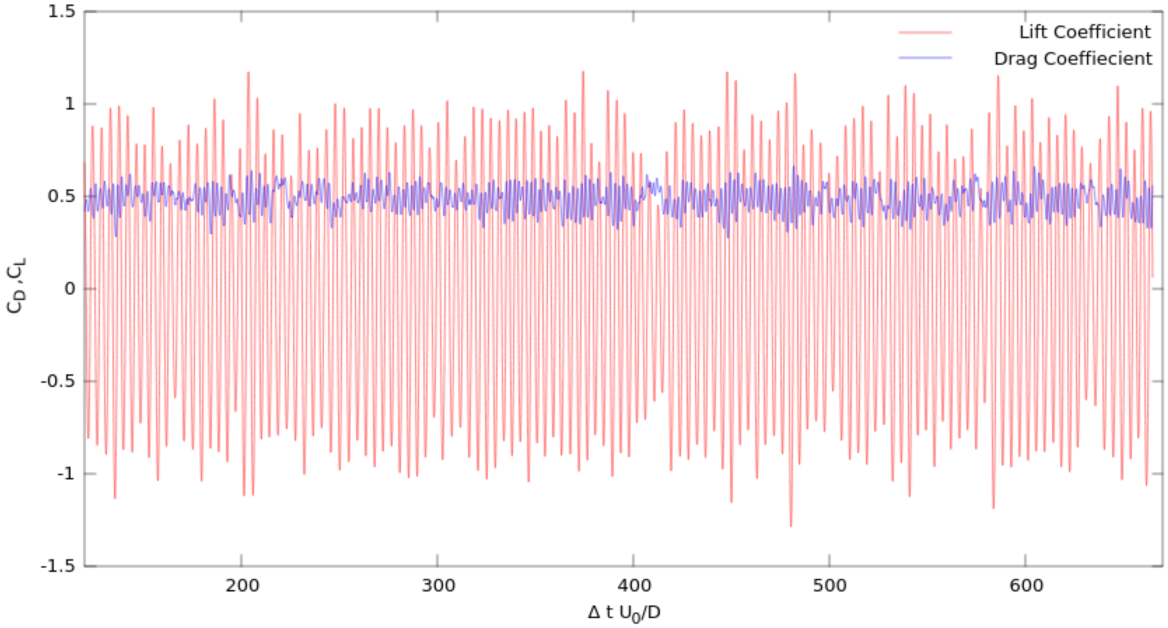

(b) Downstream Cylinder

Figure 19: Modelled histories of the lift and drag coefficients of the cylinders

5.2.3 Hydrodynamic Field

Mean velocity field

Flow was simulated to ensure turbulent separation on the surface of the upstream cylinder, it is observed that the downstream cylinder is submerged into the upstream cylinder turbulent wake. Figure 20 shows the streamlines and time-averaged velocity magnitude contours for two different states observed in Lockard [16]. State 1 is observed in the experiment where the wake from the upstream cylinder closes in the gap region, and the cylinders shed independently. In State 2 however, the wake of the upstream cylinder attaches to the downstream cylinder, and they act as a single body to the flow. State 2 was observed in the BART experiments, but only for much shorter cylinder separation distances. Lockard et al. [16] also note that other experiments at different Reynolds numbers and cylinder span lengths have observed State 2 with $S = 3.7D$.

According to Lockard et al. [16] the grid, choice of turbulence model and numerical implementation are all playing a role in determining what state a simulation develops. The choice of grid was investigated through a mesh sensitivity study, beginning with a 2-D case setup. As the mesh resolution is increased from coarse to fine, the solution tends to the experimental result. The results show that the upstream cylinder recirculation bubble is underpredicted. This is to be expected as the spanwise contributions are not being factored in. The mean velocity downstream from $x/D \approx 0.8$ is over predicted, this is due to too high a entrainment rate of free-stream flow into the gap region [17]. Next, the affect of spanwise contributions was considered. Both results underpredicts the normalized streamwise velocity suggesting that the wake from the upstream cylinder is not detached from the downstream cylinder. Hence the implemented model tends to state 2 as shown by figure 21(c). The normalised streamwise velocity achieves better agreement with experimental data when measuring the wake of the downstream cylinder as shown in figure 22(b).

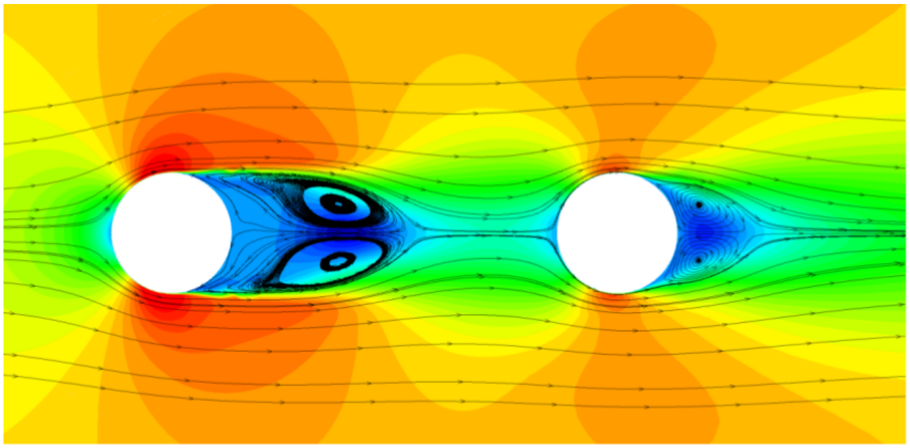

(a) State 1

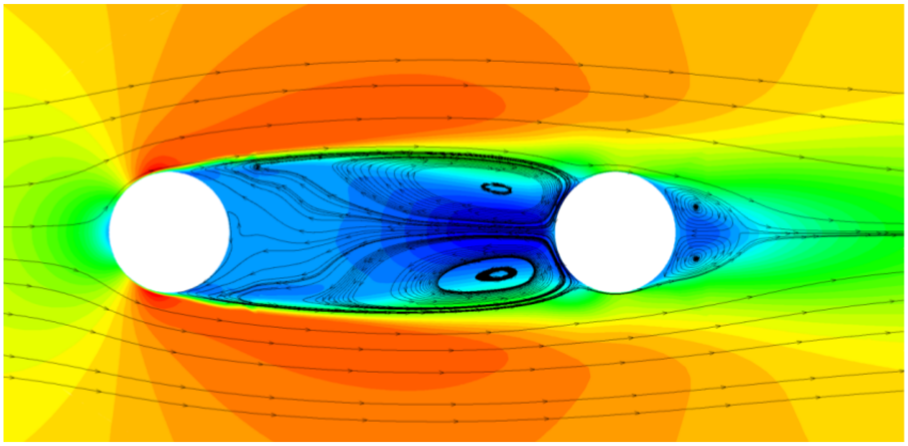

(b) State 2

Figure 20: Lockard et al. [16] observed that two states are possible with the $S = 3.7D$ configuration

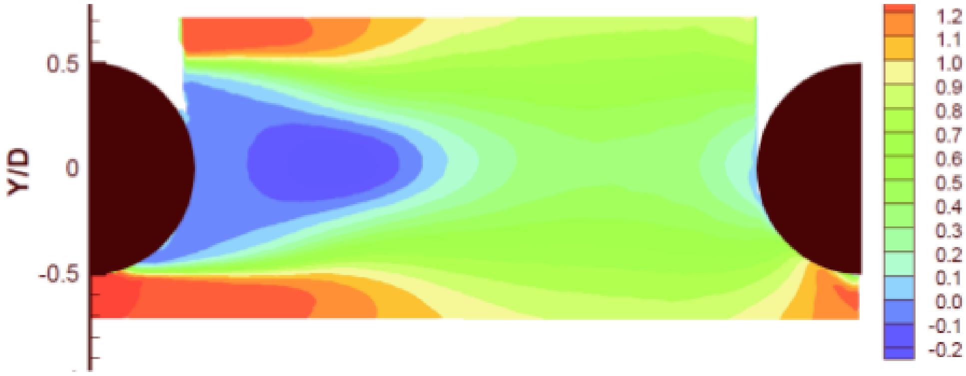

(a) BART particle image velocimetry(PIV) experimental results

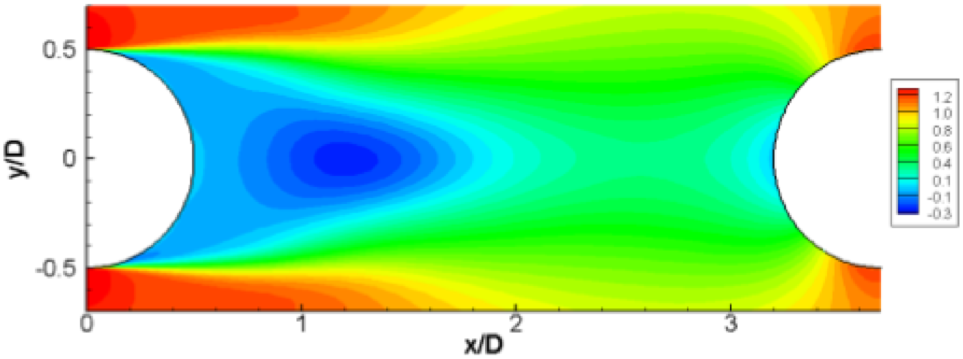

(b) Weinneman et al. [15] IDDES

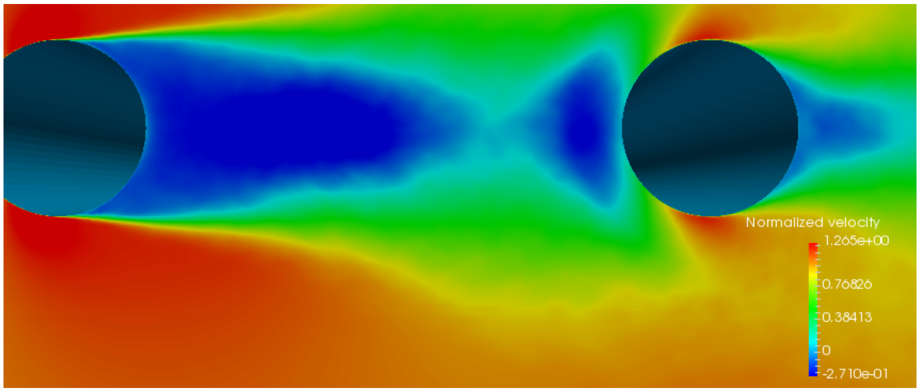

(c) Modelled IDDES

Figure 21: Normalised streamwise velocity $\frac{U}{U_0}$

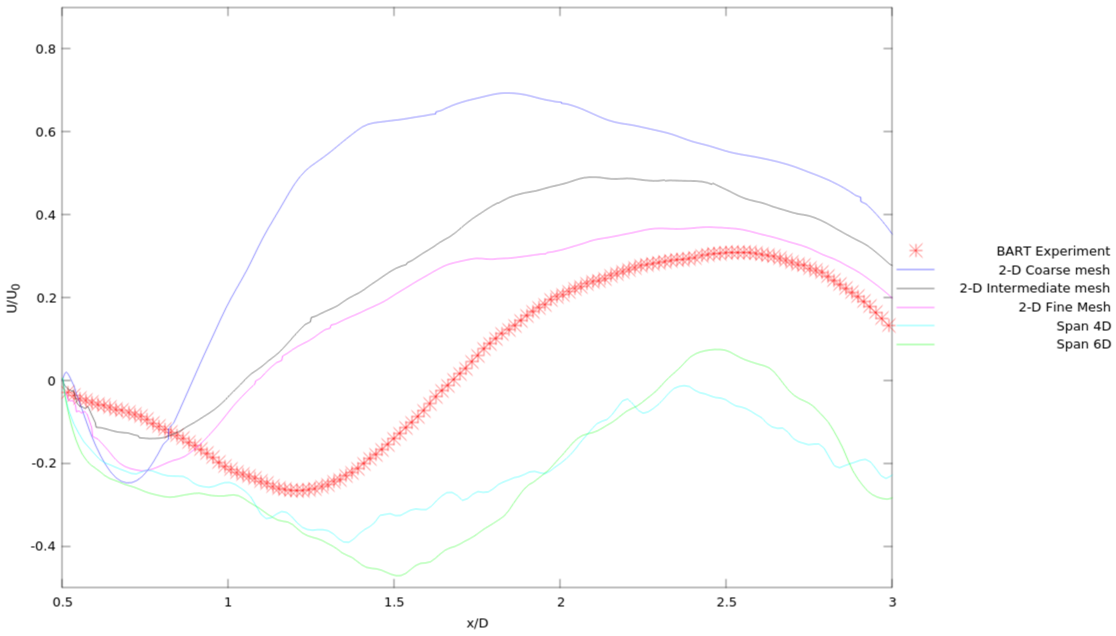

(a) Mean velocity between cylinders

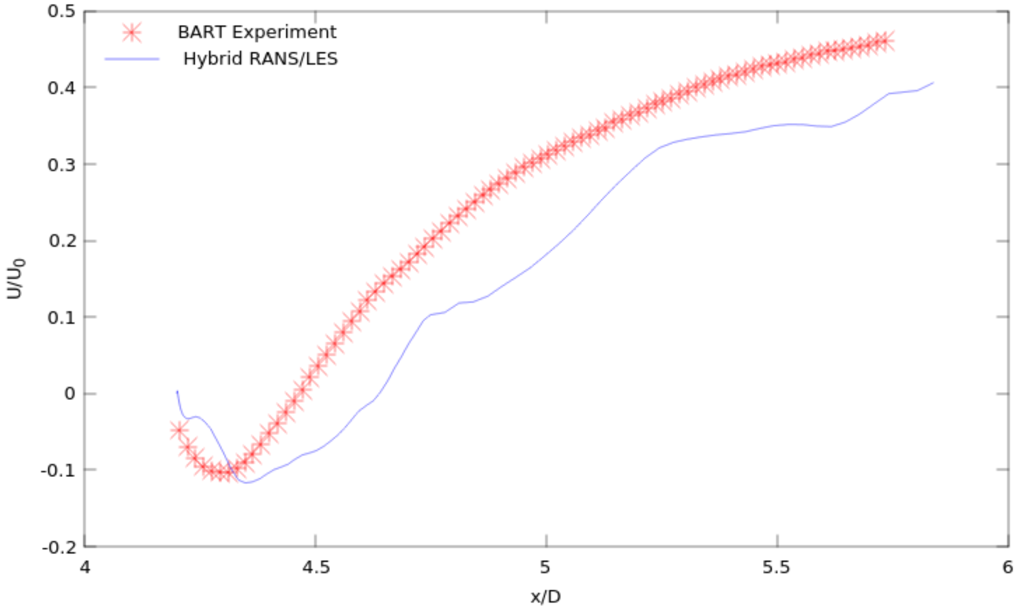

(b) Mean velocity after downstream cylinder

Figure 22: Mean velocity $\frac{U}{U_0}$ at the centreline $y = 0$.

Mean surface pressure distributions

The predicted C_p distribution over the surface of both cylinders for each simulation is provided in figure 23. The plots show that the implemented turbulence model captured the surface pressure distribtion well. The upstream cylinder C_p distribution tends towards the QFF experimental results. This is because the simulation velocity was matched to the QFF experiemnt velocity of $43.4m/s$, which is slightly different to the BART experiment velocity of $44m/s$. The C_p distribution over the downstream cylinder reflects interaction effects due to the the upstream cylinder vortex shedding in the wake.

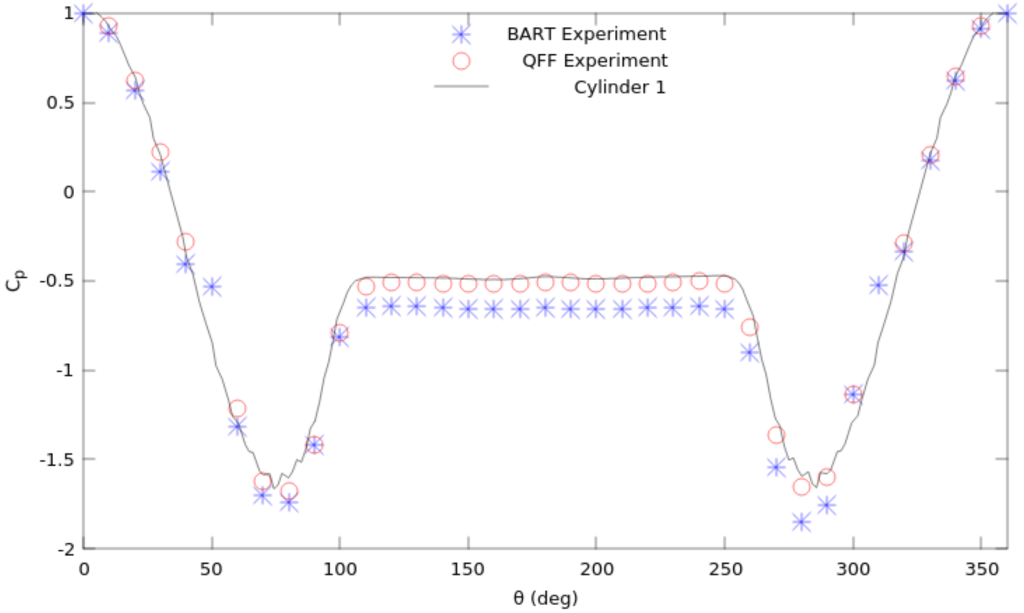

(a) Mean surface pressure distribution for the upstream cylinder

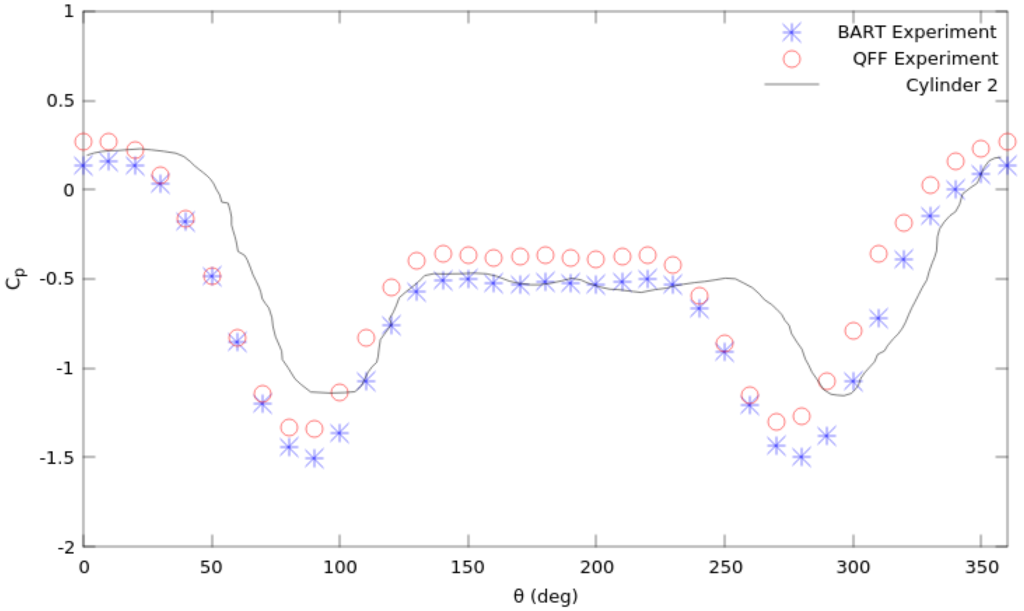

(b) Mean surface pressure distribution for the downstream cylinder

Figure 23: Modelled mean surface pressure coefficient C_p with results compared to experimental results of Jenkins et al. [11] [12] and Neuhart et al. [13].

Instantaneous flow field

A vortex can be described as a circular motion in a fluid. The difficulty in defining what vortices are lies in our intuitive concept of a vortex. The problem is exacerbated when looking at a vortex as a finite structure but it is difficult to agree on where the vortex ends [57]. The discovery of vortical structures in turbulence has resulted in a variety of methods designed to identify vortices given the output of numerical simulations or velocity measurements in experiments [58] , [59].

In this study Q-criterion of Hunt et al. [60] is used to show turbulent vorticity. The Q-criterion defines a vortex as a connected fluid region with a positive second invariant of the velocity-gradient tensor $D_{ij} = \frac{\partial u_i}{\partial x_j}$ i.e. $Q > 0$. Since this is a second order tensor, it can be decomposed into a symmetric and a skew-symmetric part as:

$$D_{ij} = S_{ij} + \Omega_{ij} \tag{59}$$

Where $S_{ij} = \frac{1}{2}\left(\frac{\partial u_i}{\partial x_j} + \frac{\partial u_j}{\partial x_i}\right)$ and $\Omega_{ij} = \frac{1}{2}\left(\frac{\partial u_i}{\partial x_j} - \frac{\partial u_j}{\partial x_i}\right)$. S_{ij} is referred to as the rate-of-strain tensor and Ω_{ij} is the vorticity tensor. The second invariant of the velocity-gradient tensor is given by:

$$Q = \frac{1}{2}\left(||\Omega_{ij}||^2 - ||S_{ij}||^2\right) \tag{60}$$

By the definition of the second invariant it is noted that in incompressible flow Q is a local measure of the excess rotation rate relative to the rate-of-strain [58]. Figure 24 shows the modelled instantaneous vorticity contours.

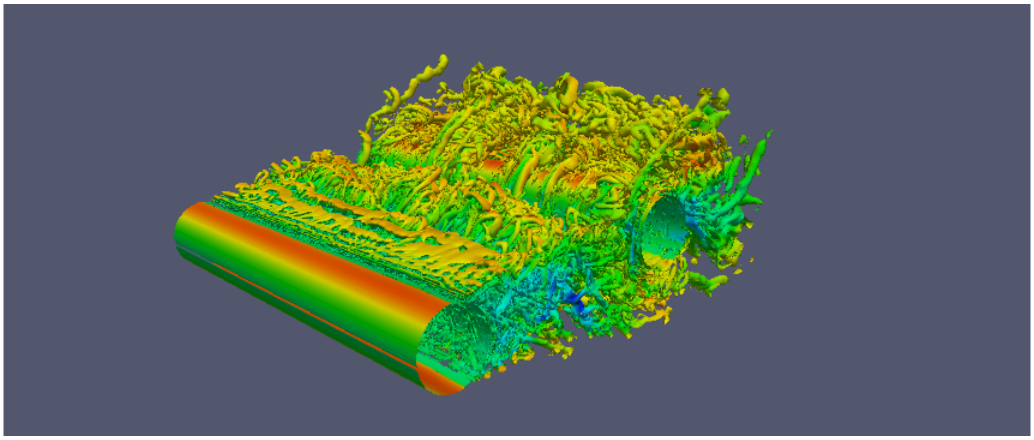

(a) Modellled IDDES with a spanwise extend of $z/D = 6$

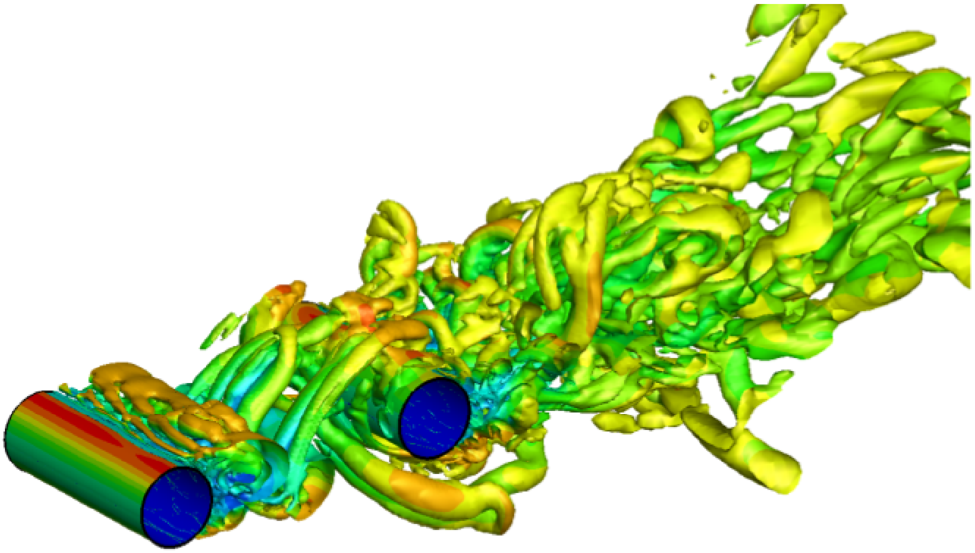

(b) Weinneman et al. [15] IDDES with a spanwise extend of $z/D = 3$

Figure 24: Instantaneous vorticity contours of $Q = 10^5 1/s^2$, coloured by streamwise velocity.

Table 2: This table provides the position of the microphones relative to the centre of the upstream cylinder.

Name	x/D	y/D
Microphone A	-8.33	27.817
Microphone B	9.11	32.49
Microphone C	26.55	27.815

5.2.4 Acoustic Results

The frequency at which the vortices are shed depends on the object shape and flow conditions. The dimensionless Strouhal number is a constant depending on the object shape only. Assuming a wavelength based on the cylinder diameter, D, the Strouhal number for a cylinder is given by:

$$St = \frac{fD}{U_0} \tag{61}$$

Where f is the shedding frequency and U_0 is the freestream velocity. The cylinders primary shedding frequency of 178 Hz was low and the experimental pole mounted microphones were only about one wavelength from the model [18]. The experimental primary shedding frequency corressponds to a Strouhal number of $St = 0.23455$, and all higher modes are harmonics of this fundamental frequency.

Table 2 provides co-ordinates, relative to the centre if the upstream cylinder, of the microphones. These microphones were located outside of the jet flow and were used to collect acoustic data. As shown in figure 25, Microphone A is slightly upstream of the model at (-8.33D, 27.815D). Microphone B is slightly downstream at (9.11D, 32.49D), and microphone C is further downstream at (26.55D, 27.815D).

Weinneman et al. [15] performed an IDDES simulation on cylinders in tandem on OpenFOAM, they used a compact form of Curle's analogy which considers only surface contributions and uses strictly time derivatives given by:

$$4\pi c_0^2 \left(\rho(\tilde{x}, t) - \rho_0\right) = \frac{1}{c_0} \iint_S \frac{x_i}{r^2} \frac{\partial}{\partial t} l_i \left[p\delta_{ij}\right] \mathrm{d}S(\tilde{y}) \tag{62}$$

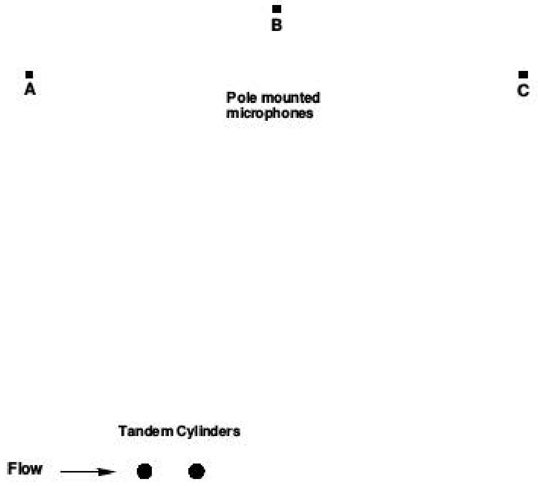

Figure 25: The positions of the microphones corresponds to approximately one wavelength at the fundamental shedding tone [17].

where $\tilde{y}$ denotes a point on the rigid surface, separated from the observation point $\tilde{x}$ by the distance r. Figure 26 shows their acoustic results. It is noted that they neglect volume(quadrupole) sources and their case shows good agreement about the main tone. However, the secondary peaks are not well captured. In addition to this, their simulated broadband levels deviate from the experimental measurements above $St = 1$.

Figure 27 and 28 show the acoustic results of the modified analogies. The primary vortex shedding tone, the resulting harmonic tones and the broadband noise up to a Strouhal number of two are well captured.

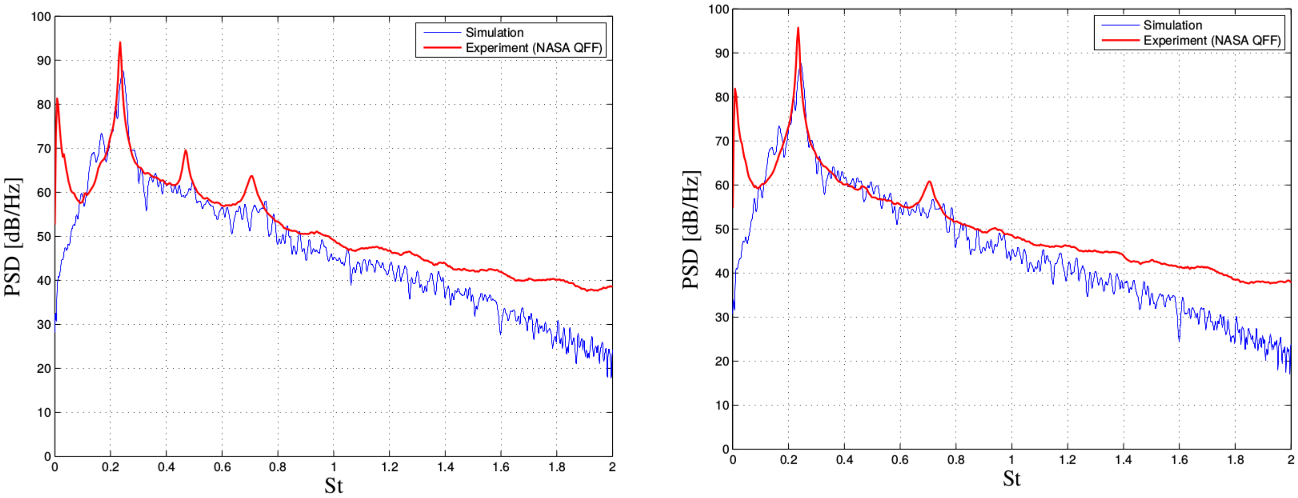

(a) Microphone A

(b) Microphone B

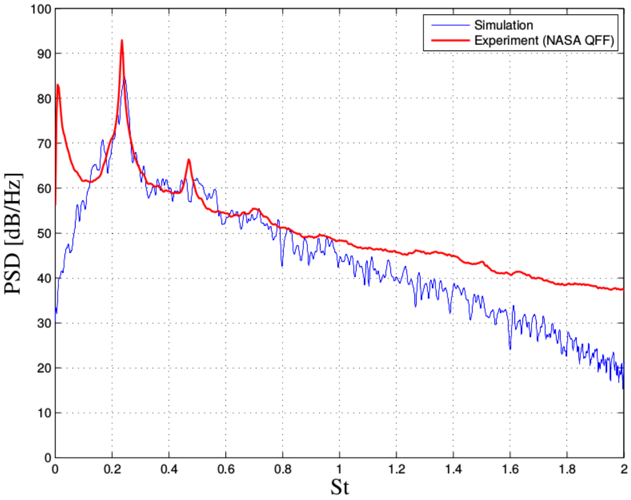

(c) Microphone C

Figure 26: Weinmann et al. [15] acoustic data from microphones A, B and C with frequency resolution $\Delta f = 5.54$, obtained using an IDDES turbulence model on OpenFOAM. Experimental data was obtained in NASAs Quiet Flow Facility [18].

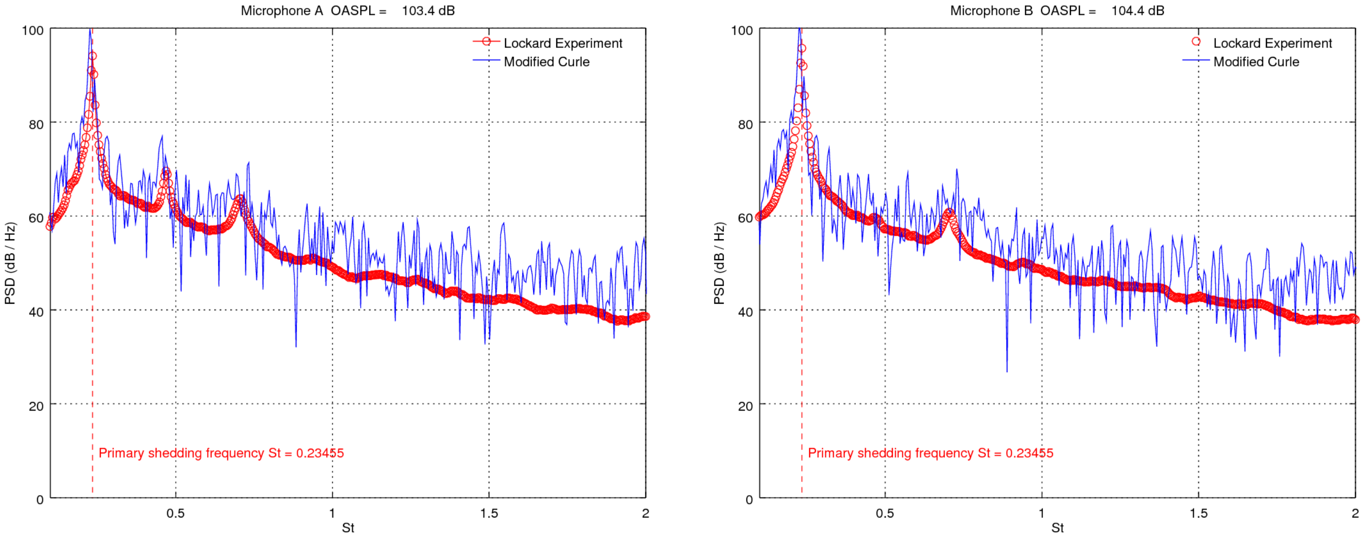

(a) Microphone A

(b) Microphone B

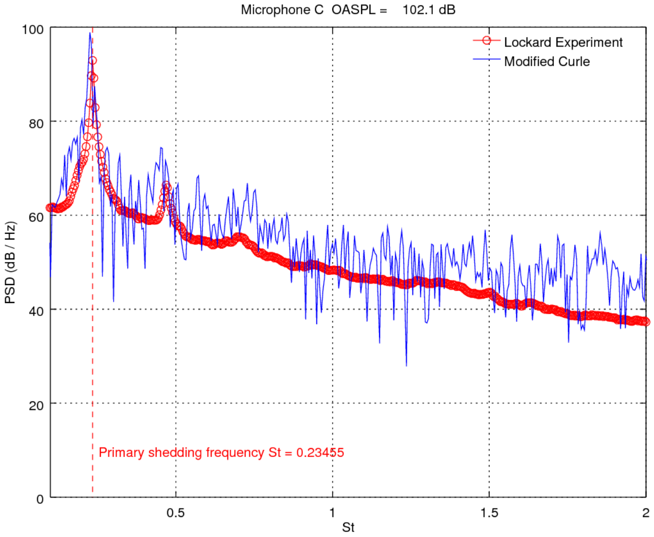

(c) Microphone C

Figure 27: Comparison of simulated modified Curles analogy and experimental acoustic results for Microphones A, B and C with frequency resolution $\Delta f = 3.8147$. Experimental data was obtained in NASAs Quiet Flow Facility [18].

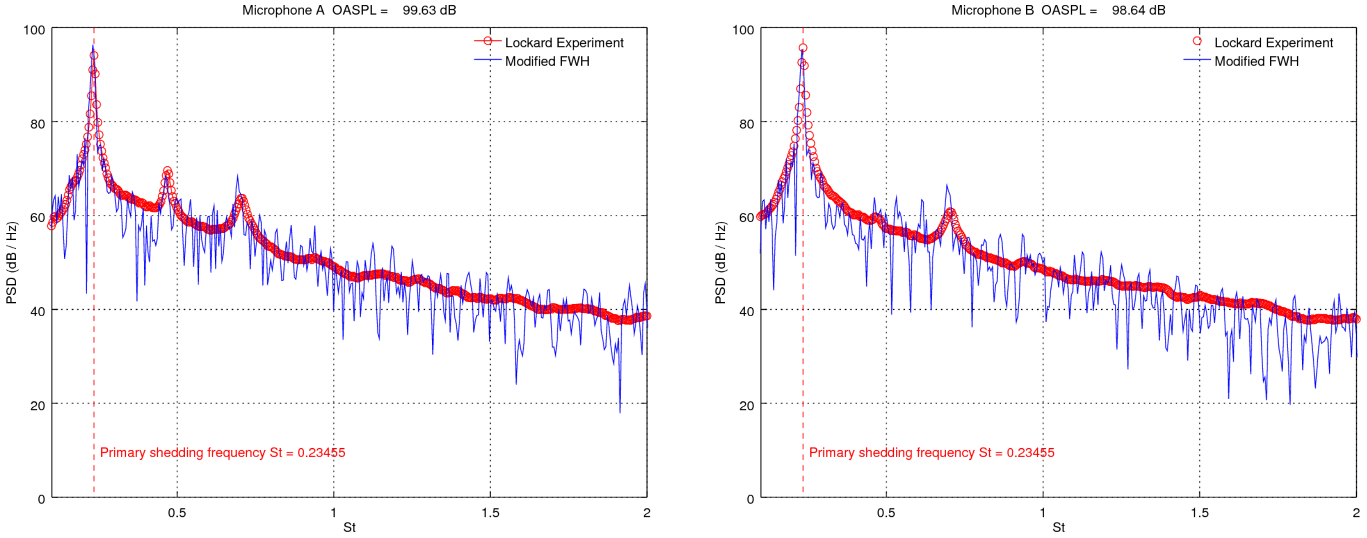

(a) Microphone A (b) Microphone B

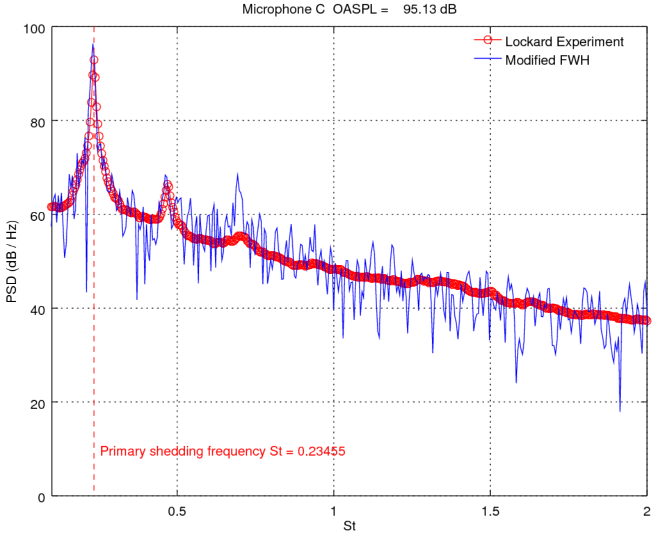

(c) Microphone C

Figure 28: Comparison of simulated modified FW-H analogy and experimental acoustic results for Microphones A, B and C with frequency resolution $\Delta f = 3.8147$.

6 Conclusion And Recommendations for Future Work

In this chapter the research conducted is summarised with reference to the aims and objectives laid out at the start of the thesis. The chapter will also discuss areas of research that could be considered for future work.

6.1 Hybrid RANS/LES Implementaion

The performance of a hybrid RANS/LES IDDES model for flow and noise predictions of the tandem cylinder experiment was investigated. The purpose of the hybrid model was to transform the baseline RANS model into a turbulence resolving subgrid scale model. The mean results between the cylinders differed from the experimental results. This is due to the chosen grid, turbulence and numerical model which did not close in the gap region. This prevented the cylinders from shedding independently, instead the wake from the upstream cylinder attached to the downstream cylinder, and the cylinders acted as a single body to the flow.

6.2 Modified Acoustic Analogies

The modified acoustic analogies provide good agreement with experimental acoustic power spectral densities measured at NASA's Quiet Flow Facility. The turbulent and unsteady wake that impinged on the surface of the downstream cylinder lead to higher surface pressure fluctuations and therefore a slightly higher predicted far-field noise. The results demonstrated the capability to predict the broadband noise of $St \geq 1$. The implemented codes explicitly (Curle) and implicitly (FW-H) factored volume (quadrupole) sources and showed good agreement with experimental data. Further research is required to establish if this is the core reason why the secondary peaks as well as the broadband noise levels are well captured.

6.3 Recommendations for Future Work

Further investigation into the causes of the second state of figure 19 (b) is recommended. As pointed out by Lockard et al [16] there are varying reasons for this and it has not been characterised in a systematic way. Upon further investigation it was found that Yang and Harris [61] mitigated this problem by using a vertex centred, 3rd order U-MUSCL (Monotonic

Upstream-Centered Scheme for Conservation Laws) scheme. This was shown to improve the solution by a factor of eight resulting in much better agreement with experimental data.

References

[1] J Larsson, L Davidson, M Olsson, and L-E Eriksson. Aeroacoustic investigation of an open cavity at low mach number. *AIAA journal*, 42(12):2462–2473, 2004.

[2] KS Brentner and F Farassat. Modeling aerodynamically generated sound of helicopter rotors. *Progress in Aerospace Sciences*, 39(2):83–120, 2003.

[3] LC Chow, K Mau, and H Remy. Landing gears and high lift devices airframe noise research. *AIAA paper*, 2408:2002, 2002.

[4] W Dobrzynski, LC Chow, P Guion, and D Shiells. Research into landing gear airframe noise reduction. *AIAA paper*, 2409:2002, 2002.

[5] B Nebenführ. Aerodynamic and aeroacoustic analysis of a multi-element airfoil using hybrid rans/les modeling approaches. 2012.

[6] E Peers. *Physics-based aeroacoustic modelling of bluff-bodies.* PhD thesis, University of Southampton, 2009.

[7] E De Villiers. *The potential of large eddy simulation for the modelling of wall bounded flows.* PhD thesis, University of London, 2007.

[8] D Parkhi. Aeroacoustics of cavity flow using time-resolved particule image velocimetry. *Master of Science Thesis*, 2009.

[9] D Coles. The law of the wake in the turbulent boundary layer. *Journal of Fluid Mechanics*, 1(02):191–226, 1956.

[10] D Coles. The turbulent boundary layer in a compressible fluid. *Physics of Fluids (1958-1988)*, 7(9):1403–1423, 1964.

[11] L Jenkins, M Khorrami, M Choudhari, and C McGinley. Characterization of unsteady flow structures around tandem cylinders for component interaction studies in airframe noise. In *11th AIAA/CEAS Aeroacoustics Conference*, page 2812, 2005.

[12] L Jenkins, D Neuhart, C McGinley, M Khorrami, and M Choudhari. Measurements of unsteady wake interference between tandem cylinders. In *36th AIAA fluid dynamics conference and exhibit*, page 3202, 2006.

[13] D Neuhart, L Jenkins, M Choudhari, and M Khorrami. Measurements of the flowfield interaction between tandem cylinders. In *15th AIAA/CEAS Aeroacoustics Conference (30th AIAA Aeroacoustics Conference)*, page 3275, 2009.

[14] MP Rumpfkeil, DK Robertson, and MR Visbal. Comparison of aerodynamic noise propagation techniques. In *52nd AIAA Aerospace Sciences Meeting*, pages 2014–0021, 2014.

[15] M Weinmann, RD Sandberg, and CJ Doolan. Flow and noise predictions for a tandem cylinder configuration using novel hybrid rans/les approaches. In *16th CEAS/AIAA Aeroacoustics Conference*, 2010.

[16] D Lockard. Summary of the tandem cylinder solutions from the benchmark problems for airframe noise computations-i workshop. In *49th AIAA Aerospace Sciences Meeting including the New Horizons Forum and Aerospace Exposition*, page 353, 2011.

[17] CJ Doolan. Flow and noise simulation of the nasa tandem cylinder experiment using openfoam. *AIAA paper*, 3157:2009, 2009.

[18] DP Lockard, MR Khorrami, MM Choudhari, FV Hutcheson, TF Brooks, and DJ Stead. Tandem cylinder noise predictions. *AIAA paper*, 3450:2007, 2007.

[19] R Girvin. Aircraft noise-abatement and mitigation strategies. *Journal of Air Transport Management*, 15(1):14–22, 2009.

[20] VL Rlumenthal, JM Streckenbach, and RB Tate. Aircraft environmental problems. *Journal of Aircraft*, 10(9):529–537, 1973.

[21] T Colonius and SK Lele. Computational aeroacoustics: progress on nonlinear problems of sound generation. *Progress in Aerospace sciences*, 40(6):345–416, 2004.

[22] HH Hubbard. Aeroacoustics of flight vehicles: Theory and practice. volume 1. noise sources. Technical report, DTIC Document, 1991.

[23] IJ Delfs. Grundlagen der aeroakustik (basics of aeroacoustics). 2014.

[24] JS Gibson. Non-engine aerodynamic noise investigation of a large aircraft. 1974.

[25] R Ewert and W Schröder. Acoustic perturbation equations based on flow decomposition via source filtering. *Journal of Computational Physics*, 188(2):365–398, 2003.

[26] D Yang, M Wang, S Chen, and X Ma. *A Fourth-Order Runge-Kutta Method with Low Numerical Dispersion for Simulating 3D Wave Propagation.* INTECH Open Access Publisher, 2011.

[27] JP Thomas and L Roe. Development of non-dissipative numerical schemes for computational aeroacoustics. *Ann Arbor*, 1001:48109–2140, 1993.

[28] CKW Tam. Computational aeroacoustics-issues and methods. *AIAA journal*, 33(10):1788–1796, 1995.

[29] J Nilsson. Implementation of acoustical analogies in openfoam and calfem. *University of Lund, Sweden*, 2010.

[30] J Lighthill. A general introduction to aeroacoustics and atmospheric sound. In *Computational Aeroacoustics*, pages 3–38. Springer, 1993.

[31] HK Versteeg and W Malalasekera. *An introduction to computational fluid dynamics: the finite volume method*. Pearson Education, 2007.

[32] D König, SR Koh, W Schröder, and M Meinke. Slat noise source identification. In *15th AIAA/CEAS Aeroacoustics Conference, AIAA-Paper*, volume 3100, 2009.

[33] JP Boris, FF Grinstein, ES Oran, and RL Kolbe. New insights into large eddy simulation. *Fluid dynamics research*, 10(4-6):199–228, 1992.

[34] M Terracol, E Manoha, and B Lemoine. Investigation of the unsteady flow and noise sources generation in a slat cove: hybrid zonal rans/les simulation and dedicated experiment. *AIAA Paper*, 3203:2011, 2011.

[35] DW Zingg and P Godin. A perspective on turbulence models for aerodynamic flows. *International journal of computational fluid dynamics*, 23(4):327–335, 2009.

[36] JS Cox, KS Brentner, and CL Rumsey. Computation of vortex shedding and radiated sound for a circular cylinder: subcritical to transcritical reynolds numbers. *Theoretical and Computational Fluid Dynamics*, 12(4):233–253, 1998.

[37] JD Revell and GJ Healy. Methods for the prediction of airframe noise. *AIAA paper*, 3157:75–539, 2009.

[38] FJ Souliez, LN Long, PJ Morris, and A Sharma. Landing gear aerodynamic noise prediction using unstructured grids. *International Journal of Aeroacoustics*, 1(2):115–135, 2002.

[39] R Ewert and W Schröder. On the simulation of trailing edge noise with a hybrid les/ape method. *Journal of Sound and Vibration*, 270(3):509–524, 2004.

[40] O Verhoeven. *Trailing edge noise simulations*. PhD thesis, Masters thesis, Delft University of Technology, 2011.

[41] A Hirschberg and SW Rienstra. An introduction to aeroacoustics. *Eindhoven university of technology*, 2004.

[42] N Curle. The influence of solid boundaries upon aerodynamic sound. In *Proceedings of the Royal Society of London A: Mathematical, Physical and Engineering Sciences*, volume 231, pages 505–514. The Royal Society, 1955.

[43] JEF Williams and DL Hawkings. Sound generation by turbulence and surfaces in arbitrary motion. *Philosophical Transactions of the Royal Society of London A: Mathematical, Physical and Engineering Sciences*, 264(1151):321–342, 1969.

[44] S. Sarkar and MY Hussaini. *Computation of the Acoustic Radiation from Bounded Homogeneous Flows*, pages 335–355. Springer New York, New York, NY, 1993.

[45] J Schmalz and W Kowalczyk. Determination of acoustic parameters in flow fields using openfoam. *PAMM*, 14(1):707–708, 2014.

[46] FR Menter, M Kuntz, and R Langtry. Ten years of industrial experience with the sst turbulence model. *Turbulence, heat and mass transfer*, 4(1):625–632, 2003.

[47] PR Spalart and SR Allmaras. A one equation turbulence model for aerodinamic flows. *AIAA journal*, 94, 1992.

[48] S Deck, P Duveau, P d'Espiney, and P Guillen. Development and application of spalart–allmaras one equation turbulence model to three-dimensional supersonic complex configurations. *Aerospace Science and Technology*, 6(3):171–183, 2002.

[49] ML Shur, PR Spalart, MKh Strelets, and AK Travin. A hybrid rans-les approach with delayed-des and wall-modelled les capabilities. *International Journal of Heat and Fluid Flow*, 29(6):1638–1649, 2008.

[50] C Hirsch. *Numerical computation of internal and external flows: The fundamentals of computational fluid dynamics*. Butterworth-Heinemann, 2007.

[51] H Jasak. Error analysis and estimation for finite volume method with applications to fluid flow. 1996.

[52] RI Issa. Solution of the implicitly discretised fluid flow equations by operator-splitting. *Journal of computational physics*, 62(1):40–65, 1986.

[53] T Gandhi. Numerical investigation of aeroacoustic interaction in the turbulent subsonic fow past an open cavity. 2010.

[54] JM McDonough. Lectures on turbulence. *University of Kentucky*, 2007.

[55] DB DeGraaff, DR Webster, and JK Eaton. The effect of reynolds number on boundary layer turbulence. *Experimental Thermal and Fluid Science*, 18(4):341–346, 1998.

[56] AK Pancham. *Flow over a partially liquid filled cavity.* PhD thesis, TU Delft, Delft University of Technology, 2014.

[57] V Holmén. Methods for vortex identification. *Masters Theses in Mathematical Sciences*, 2012.

[58] P Chakraborty, S Balachandar, and RJ Adrian. On the relationships between local vortex identification schemes. *Journal of Fluid Mechanics*, 535:189–214, 2005.

[59] V Kolar. Brief notes on vortex identification. *Recent Advances in Fluid Mechanics, Heat & Mass Transfer and Biology WSEAS*, 2007.

[60] J Hunt, A Wray, and P Moin. Eddies, streams, and convergence zones in turbulent flows. 1988.

[61] HQ Yang and RE Harris. Vertex-centered, high-order schemes for turbulent flows. In *54th AIAA Aerospace Sciences Meeting*, page 1098, 2016.